FIBER OPTIC STRAIN GAUGE CALIBRATION AND DYNAMIC FLEXIBILITY TRANSFER FUNCTION IDENTIFICATION IN MAGNETIC BEARINGS

A Thesis

by

ZACHARY SCOTT ZUTAVERN

Submitted to the Office of Graduate Studies of
Texas A&M University
in partial fulfillment of the requirements for the degree of

MASTER OF SCIENCE

May 2004

Major Subject: Mechanical Engineering

FIBER OPTIC STRAIN GAUGE CALIBRATION AND DYNAMIC FLEXIBILITY TRANSFER FUNCTION IDENTIFICATION IN MAGNETIC BEARINGS

A Thesis

by

ZACHARY SCOTT ZUTAVERN

Submitted to Texas A&M University
in partial fulfillment of the requirements
for the degree of

MASTER OF SCIENCE

Approved as to style and content by:

Dara Childs (Chair of Committee)	Alan Palazzolo (Member)
Henry Taylor (Member)	Dennis O'Neal (Head of Department)

May 2004

Major Subject: Mechanical Engineering

ABSTRACT

Fiber Optic Strain Gauge Calibration and Dynamic Flexibility Transfer Function Identification in Magnetic Bearings. (May 2004)

Zachary Scott Zutavern , B.S., Texas A&M University;

B.A., Texas A&M University

Chair of Advisory Committee: Dr. Dara Childs

Historical attempts to measure forces in magnetic bearings have been unsuccessful as a result of relatively high uncertainties. Recent advances in the strain-gauge technology have provided a new method for measuring magnetic bearing forces. Fiber optic strain gauges are roughly 100 times more sensitive than conventional strain gauges and are not affected by electro-magnetic interference. At the Texas A&M Turbomachinery Laboratory, installing the fiber-optic strain gauges in magnetic bearings has produced force measurements with low uncertainties. Dynamic flexibility transfer functions exhibiting noticeable gyroscopic coupling have been identified and compared with results of a finite element model. The comparison has verified the effectiveness of using magnetic bearings as calibrated exciters in rotordynamic testing. Many applications including opportunities for testing unexplained rotordynamic phenomena are now feasible.

To my wife, Lauren, for her love and support.

To my parents for always making my education a priority.

ACKNOWLEDGEMENTS

I would like to thank Dr. Dara Childs for this exceptional research opportunity and for his support and guidance in my education. Stephen Phillips and Eddie Denk were also invaluable with their involvement in this project. I appreciate the willingness of Dr. Alan Palazzolo and Dr. Henry Taylor to serve on my thesis committee. The talented efforts of previous students, Stephen Raymer and Luca Pavesi, allowed me to utilize their research and continue on with the project. Finally, thanks to the Turbomachinery Research Consortium, whose support made this project possible.

NOMENCLATURE

$\mathbf{B}$	Input matrix []
b	Rotor drop FOSG calibration intercept [b]
$\mathbf{C}$	FOSG calibration matrix [N V^{-1}] or output matrix []
C	Current-position formula calibration factor [N μm^2 A^{-2}]
E	Modulus of elasticity [Pa]
$\mathbf{F}$	Magnetic bearing force matrix [N]
F	Magnetic bearing force [N]
$F_{uncalibrated}$	Uncalibrated force factor [A^2 μm^{-2}]
F_0	Current-position formula tare force [N]
f	Injection frequency [Hz], or rotor reaction force [N]
$\mathbf{G}$	Flexibility matrix [μm N^{-1}]
G	Flexibility [μm N^{-1}]
g	Current-position formula effective gap parameter [μm]
$\mathbf{I}$	Moment of inertia matrix [kg m^2]
I_A	Area moment of inertia [m^4]
I_{bottom}	Bottom pole current [A]
I_{top}	Top pole current [A]
I_1	Rotor polar moment of inertia [kg m^2]
I_2	Rotor radial moment of inertia [kg m^2]
K	Stiffness [N μm^{-1}]
k	FOSG calibration coefficient [N V^{-1}]
L	Shaft length [m]
l	Distance between magnetic bearings [m]
l_{cg}	Distance from drive-end magnetic bearing to CG of rotor [m]
m	Rotor mass [kg]
r_I	Inertia ratio []
r_m	Mass ratio []
s	FOSG calibration slope [N V^{-1}]
$\mathbf{V}$	FOSG SCU voltage matrix [V]
V	FOSG SCU output voltage [V]
W	Rotor weight [N]
$\mathbf{X}$	Position matrix [μm]
w	External weight [N]
X	Horizontal position [m]
X_0	Injection amplitude [μm]
x	Rotor position [μm]
Y	Vertical position [m]
α	Angular acceleration vector [rad s^{-1}]
β	Time scaling factor [s^{-1}]
Δx_{actual}	Actual rotor displacement [μm]

$\Delta x_{detected}$	Detected rotor displacement [μm]
ϕ	Euler angle [rad s^{-1}]
$\mathbf{\Gamma}$	Torque vector [N m]
γ	Angular position scaling factor []
η	Linear position scaling factor [m^{-1}]
θ	Angle between two specified vectors or axes [rad]
τ	Rotor reaction moment [N m]
$\boldsymbol{\omega}$	Angular velocity vector [rad / s]
ω	Injection frequency [rad s^{-1}]
ω_N	Non-dimensional rotor speed []
ξ	Damping ratio []
ψ	Euler angle [rad s^{-1}]

Subscripts

bottom	Characteristic of the bottom pole
N	Non-dimensionalized variable
S1	Characteristic of FOSG S1
S2	Characteristic of FOSG S2
S3	Characteristic of FOSG S3
S4	Characteristic of FOSG S4
top	Characteristic of the top pole
X	In the *X* direction of the *X*, *Y*, *Z* coordinate system
x	Horizontal direction
Y	In the *Y* direction of the *X*, *Y*, *Z* coordinate system
y	Vertical direction
Z	In the *Z* direction of the *X*, *Y*, *Z* coordinate system

TABLE OF CONTENTS

Page

Page

LIST OF FIGURES

Page

Page

Page

LIST OF TABLES

Page

I. INTRODUCTION

Research in rotordynamics, as in other fields, relies heavily on test measurements to characterize dynamic phenomena. Rotor motions are measured with proximity probes, accelerometers, and occasionally velocimeters. These measurements can typically be determined accurately and with relative ease as compared with force measurements. Forces are typically measured with strain gauges and calibrated load cells, and they are sometimes calculated from inertial properties. By nature, forces tend to be more difficult to measure because the sensors require several features for accurate measurements. The sensors must have physical contact with the forcing mechanism. The sensors must detect, or at least accurately reflect, all relevant forces. Finally, the sensor cannot interfere with the force application, either by adding inertia, or softening the force mechanism. With rotating machinery, these requirements can be difficult to meet.

Magnetic bearings have been recognized for years as having a great potential for force measurement. The non-contact interface provides a method for applying forces directly to a rotating component. The applied force is a function of the air gap, the control current, and the magnetic properties of the materials. There have been attempts to determine the applied forces by modeling the magnetic force, by measuring the magnetic flux, and by installing load cells within the bearings. However, the levels of uncertainty in such attempts have proved excessive, and test results using these methods would likely be inconclusive.

Recent efforts at the Texas A&M University (TAMU) Turbomachinery Laboratory have focused on a new method of measuring forces in magnetic bearings. With the advent of a new fiber optic technology, strain measurements accuracy has been improved by a factor of 100. By installing these highly sensitive strain gauges in magnetic bearings, accurate force measurements can be produced. This approach opens the door for new test methods, and provides an opportunity for measuring new phenomena.

This thesis follows the style and format of the Journal of Tribology.

Technologies

Two modern technologies are utilized throughout this research: magnetic bearings and fiber optic strain gauges. Combining these technologies allows for accurate force measurements within magnetic bearings. A general description of these technologies follows.

Magnetic Bearings

Figure 1 displays the main components of a typical magnetic bearing (MB) [1]. MBs are increasingly used in rotating machinery because they offer several advantages over conventional bearings. A MB uses electrical currents to generate magnetic fields that levitate the rotor. As a result, there is no physical contact between the MBs and the rotor. This significantly reduces the power loss associated with the bearing and eliminates physical wear. Magnetic bearings can also support rotors at higher speeds than conventional bearings. Some MB machine tool spindles can rotate at speeds up to 100,000 rpm. MBs are also used in high-speed flywheel applications for energy storage. Controllability is another advantage. The bearing settings can be adjusted to produce desired characteristics and responses. In addition to varying standard parameters such as stiffness and damping, many bearing controllers have vibration control options that can produce rotating forces to counteract imbalance.

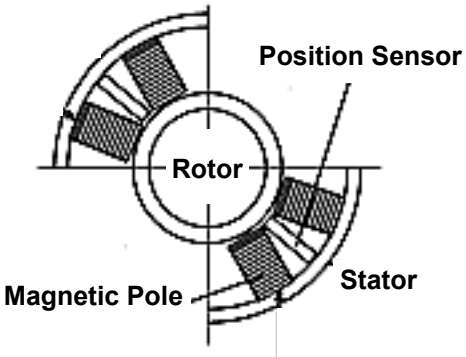

Fig. 1 Typical MB Construction [1]

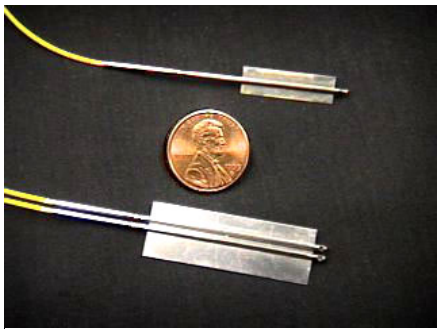

Fig. 2 Fiber Optic Strain Gauges [2]

Fiber Optic Strain Gauge Technology

Fiber optic strain gauges (FOSGs), like conventional strain gauges, measure strain in materials. One end of the fiber optic is bonded to the surface of a material. The bonded ends of two fibers are shown in Figure 2 [2]. The fiber has two reflective surfaces within the bonded region. Light is transmitted from the opposite end of the fiber to the surfaces and then reflected back, creating an interference pattern. As strain is produced in the material, the interference pattern changes, and a signal conditioning unit translates the pattern change into a voltage proportional to material strain. FOSGs have can measure strains 100 times more accurately than conventional strain gauges. The optical signals are not corrupted by electrical and magnetic noise, which is very important for the present application. By bonding the FOSGs to the poles of MBs, reaction forces between the rotor and the bearing can be determined. Other approaches toward determining magnetic bearing forces have been undertaken and are discussed in the following section.

Methods of Force Measurement

Previous attempts at force measurement in magnetic bearings have experienced limited success. Methods using magnetic flux sensors, load cells, and empirical current and position formulas have produce results with relatively large uncertainties. Using Fiber Optic Strain Gauge (FOSG) technology, the accuracy of the force measurements is substantially improved. The accuracy is sufficient to allow identification of significant system characteristics.

Piezoelectric Load Cells

Traxler and Schweitzer [3] mounted piezoelectric load cells between the interface of the magnetic bearing housings and the test platform to measure reaction forces. Displacements of the bearing housings produced inertial forces that affected the reaction-force measurements. The inertial forces were calculated using accelerometer measurements and were then subtracted from the measured total force to calculate the

actual force applied to the rotor. The signal to noise ratio was low and the inertial forces were large at higher frequencies.

Lee, Ha, and Kim [4] used a similar approach to perform system identification. They also experienced large uncertainties. In general, this approach is problematic because the load cells must be sized to properly secure the bearings and must have an acceptable sensitivity for forces generated at high frequencies. This causes the low frequency results to have a poor signal to noise ratio. The high frequency results are also suspect because the bearing motions increase with frequency and produce inertial forces.

Empirical Current and Position Formulas

Matros, Sobotzik, and Nordmann [5] used an empirical formula relating the bearing currents and the rotor position to the applied force. Their formulas neglect eddy current loss, hysteresis, and magnetic saturation effects. Matros et al. modeled hysteresis and saturation properties in an effort to improve results. The force calculations were used to determine bearing and seal coefficients. In a specific case, stiffness was over predicted by 8%.

Fittro , Baun , Maslen , and Allaire [6] measured forces on a static test rig, varying eccentricity and force amplitude. They found that eccentricity changes contributed to most of the uncertainty in the results. The mean error distribution and standard deviation were 1% and 4% of the bearing load capacity respectively.

Magnetic Flux Sensors

Gahler [7] used hall sensors to measure the magnetic flux from the bearing poles. The rotor position and magnetic flux were related to the force with an empirical formula. A correction algorithm was implemented to correct for eddy currents, hysteresis, and saturation. Dynamic forces were applied at frequencies from 20 to 200 Hz with constant amplitude, and the force error was ±11% of load capacity. Dynamic forces were then

applied at 120 Hz for various amplitudes, and the force error was reduced to ±2% of load capacity.

Knopf and Nordmann [8] used flux measurements to identify dynamic properties of hydrodynamic bearings. Uncertainties were around 1% of load capcity for static measurements, but they deteriorated to 5% with increasing eccentricity and rotor speed.

Pottie [9] used several methods to determine forces of magnetic bearings. A current and position dependent force model was attempted, and considerable time and effort was spent trying to map the model coefficients. Hall sensors were also attempted. A third method was to support the poles (not the bearing housings) with strain gauges. However the strain gauges that were sensitive enough to make accurate measurements allowed the MB poles to move. Accelerometers were installed to compensate for the pole inertial forces. Unfortunately, this introduced new vibration modes and resonances. All of these methods were unable to significantly improve uncertainties over previous methods.

Force Measurement in MBs at TAMU Turbomachinery Laboratory

Raymer and Childs [10] used FOSGs to measure dynamic forces applied by an external exciter. This method resulted in dramatic improvements in uncertainty. The uncertainty was 1 lb (4 N) or .1% of the bearing load capacity. Pavesi and Childs [11] attempted to use an empirical formula based on current and position to calibrate the FOSGs at low frequencies. The formula was believed to be sufficiently accurate at low frequencies because of the high repeatability of the results. This method encountered difficulties with a parameter in the formula, and the resulting uncertainties were not as low as in the method of Raymer and Childs.

FOSGs have produced the most promising results to date. An accurate calibration method would open the door for new research applications in rotordynamics. In the present work, a new calibration method has been developed and system properties have been determined. The Inertial Calibration Method uses dynamic calculations based on

the mass properties of the rotor to calibrate the FOSGs. Using the calibrated FOSGs, dynamic flexibility transfer functions (DFTFs) have been experimentally determined. DFTFs describe the position response of a system due the applied forces. The details of the calibration and the DFTF identification comprise the remainder of this thesis.

Test Equipment Description and Theory of Operation

The test rig consists of a rotor supported at either end by a radial magnetic bearing. The rotor is driven by an electric motor, and the system is equipped with pneumatic brakes. The FOSGs are installed in the non-drive end bearing. Data from the MB controller output and the FOSG signal conditioning unit (SCU) are acquired using National Instruments hardware and Labview software. The data reduction is performed in MS Excel. A detailed description of the test rig and data acquisition system follows.

Test Rig

The MB Test Rig is displayed in Figure 3. The magnetic bearings (1) have a load capacity of 800 lbf (3560 N) and support a steel rotor (2) weighing 400 lbf (1780 N). Disks (3) increase the rotational inertia and, accordingly, the gyroscopic coupling. The laminated sleeves (4) are the surface on which the magnetic force is exerted. Auxiliary bearings (5) support the rotor when it is not levitated. The coupling (6) and the quill

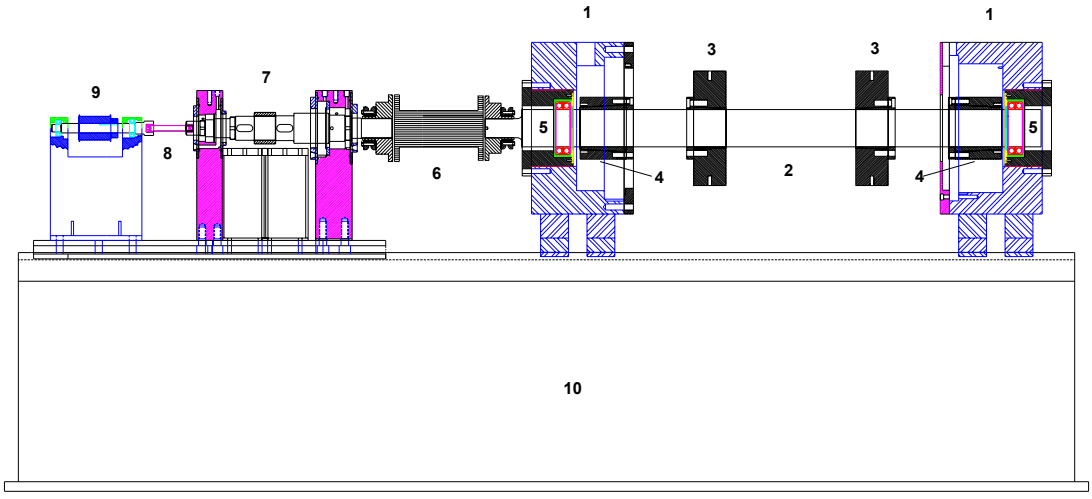

Fig. 3 Magnetic Bearing Test Rig at TAMU Turbomachinery Laboratory

shaft (8) are both shielded for safety. The brakes (7) can be used to rapidly decelerate the system if the rotor delevitates. A pulley (9) and drive belt transmit power from the motor. The test stand (10) is constructed of .75 in. (19 mm) steel plates with a 3 in. (76 mm) steel top.

NI Hardware and Labview Data Acquisition System

The data acquisition system consists of 2 E-series National Instruments PCI cards. The 6035E card has 2, 12 bit, analog output channels and 8, 16 bit, differential type analog input channels. The 6036E has 2, 16 bit, analog outputs channels and 8, 16 bit, differential type analog input channels. Each E-series card is connected to an external SC2040 card, which allows the analog inputs for each board to be acquired simultaneously. By connecting the two E-series cards with a RSTI cable, the analog input and analog output signals can be routed from one board to another. This allows for the synchronization of the analog inputs and analog outputs of both cards.

The maximum sampling rate per channel, when all channels are in use, is approximately 10 kHz. With analog inputs in use, the maximum update rate for the analog output is between 5 and 10 kHz depending on the length of time for a test. The 6036E has difficultly consistently updating at 10 kHz (with analog inputs in use) for times of 10 seconds or longer, probably because the analog outputs are 16 bit.

A test was performed to validate the data acquisition system. One analog output from each card was connected to one of its own analog inputs and one output was connect to one of the other card's inputs. This test can demonstrate the synchronization of all outputs and inputs. Sinusoids of different DC offsets with frequencies of 200 Hz were generated by each analog output. The update rates and sampling frequencies were all 10 kHz. Figure 4 displays 100 000 samples. Figure 5 shows the first 50 samples (5 ms), and Figure 6 shows the last 50 samples.

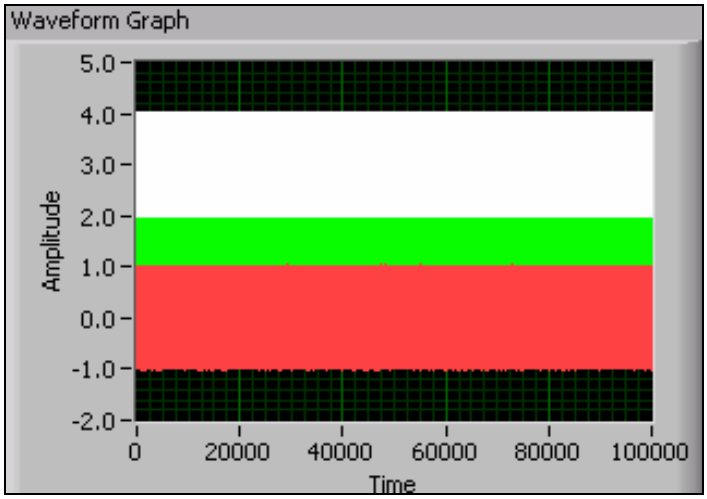

Fig. 4 100 k Samples with Sample Rates and Update Rates All 10 kHz

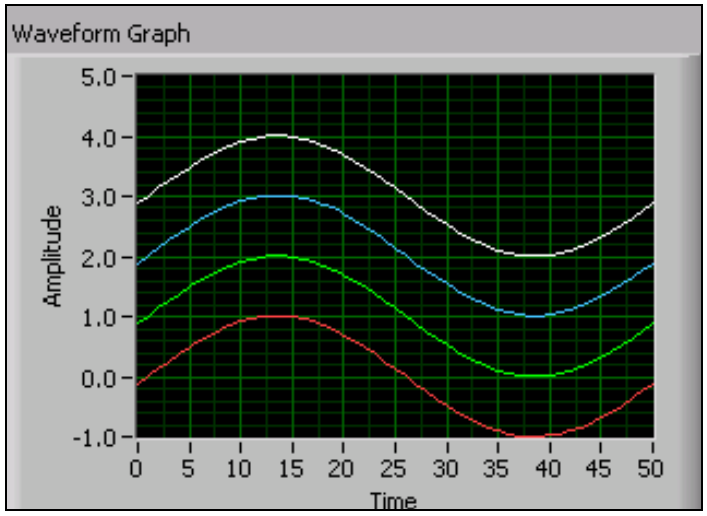

Fig. 5 First 50 Samples

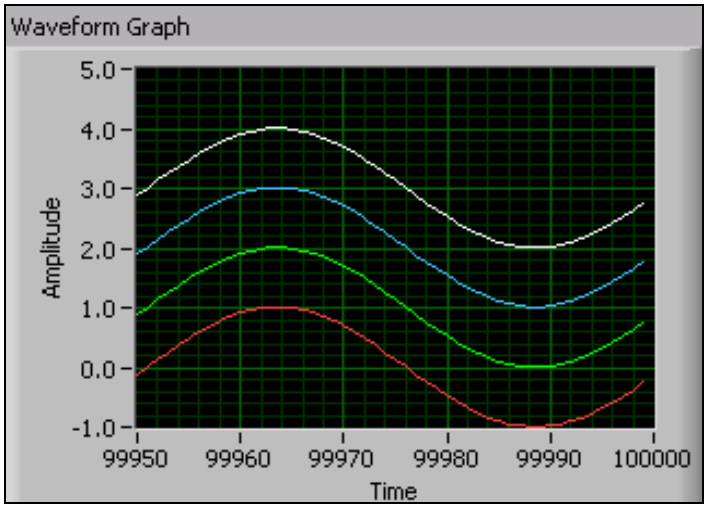

Fig. 6 Last 50 Samples

The sinusoids all appear to be clearly in phase. FFT analysis demonstrated a phase error of ± 0.02°, which, at 200 Hz, corresponds to 0.28 μs. It can also be seen from the results that the analog input values are the analog output values from the previous update, which is to be expected. In other words, the second sample (sample number 1) it is equal to the DC value of the signal. DC value of the signal is the first analog output update, occurring at the same time as sample 0.

FOSG Signal Conditioning and Theory

The FOSGs connect to the FOSG Signal Conditioning Unit (SCU). This device creates the laser light that is directed into the fiber optic cables. The light travels down the cables and reached the end where the strain gauge is bonded to the MB. Figure 7 demonstrates that the laser light is partially reflected by two surfaces typically spaced 0.47 in (12 mm) apart. The reflected light travels back through the fiber to the SCU. A Fabry-Perot interferometer technique is utilized to determine the phase shift resulting from the travel length difference of the light. The phase shift is related to the distance between the two surfaces. As the FOSG is strained, the distance between the surfaces changes, the phase of the light changes, and the strain is detected. The SCU output

voltage signals indicate the strain. The voltages are recorded by the data acquisition system.

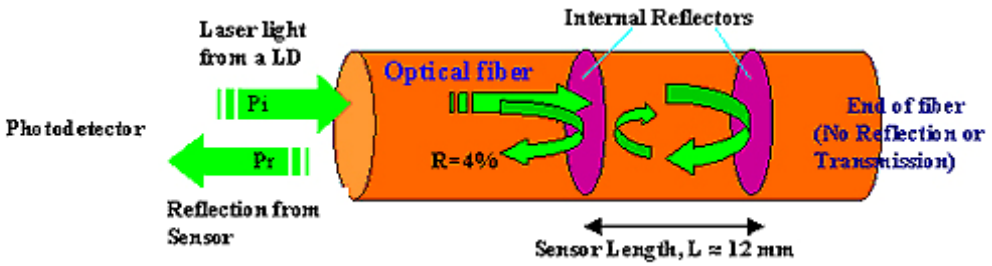

Fig. 7 Fiber Optic Strain Gauge Operation [2]

Magnetic Bearing Control Hardware and Software

The magnetic bearing controller is the MBControl module produced by Revolve Magnetic Bearings Inc. This module uses position measurements from proximity probes to determine current response required to levitate the rotor. The MBControl module controls amplifiers that produce the required currents. In addition, the module interfaces with a PC through a serial link and MBScope software that is installed on the PC. The module also creates analog ouputs through the MBResearch panel. These outputs are voltage signal that indicate rotor position and control currents. The MBResearch panel also has analog inputs that the MBControl module can use to adjust either target rotor position or the control currents. The analog input must be activated using the MBScope software.

The MBScope software has a variety of programs that adjust control settings and options, determine calibration settings, and display measurements of current, rotor position, and calculated force. These programs and their uses are discussed in detail later.

The notation used by the software is displayed in Figure 8 as seen from the drive end. The *V13* and *W13* axes coincide at the center of the drive end MB, and the *V24* and *W24* axes coincide at the non-drive MB center.

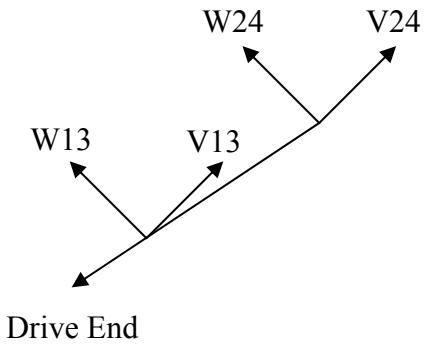

Fig. 8 Axis Notation for MBScope Software

The FOSG locations are displayed in Figure 9 as seen from the non-drive end. Each FOSG is bonded to one of the primary MB poles. These poles do not lie on the axes used by the MBs. However, each pair of primary poles and the adjacent auxiliary poles act in unison. This causes the net force exerted by a given pole to occur along an axis. The result is that the FOSG detects the net force exerted by a pole along the poles respective axis.

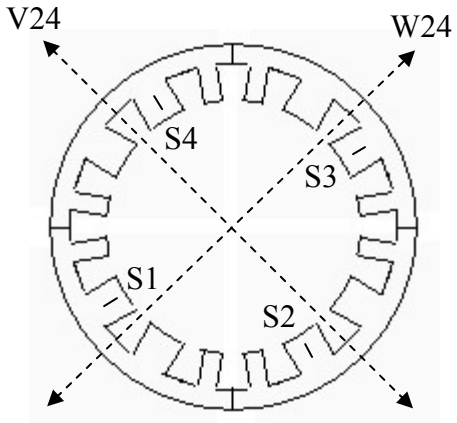

Fig. 9 FOSG Locations

II. MAGNETIC BEARING CALIBRATION

The first step in test process is to accurately calibrate the MBs. Clearly, the proximity probe calibration is essential for accurate test results. Additionally, centering the shaft within the bearing is important for improving linearity of different bearing properties, and to prevent contact with the auxiliary bearings during operation. The forces of the bearing can also be described by a formula using the control current and the rotor position. The parameters of this formula must be accurately determined because one of the FOSG calibration methods that is addressed uses formula.

Magnetic Bearing Rotor Centering

The center position of the rotor is determined by carefully bumping the rotor against the auxiliary bearings and calculating the point equidistant from the bump locations. This step is performed using the Calibration tool in the MBScope software package. The Calibration tool shown in Figure 10 displays the results from one of the bump tests. The *New Offset* is the rotor center position given in proximity probe voltage.

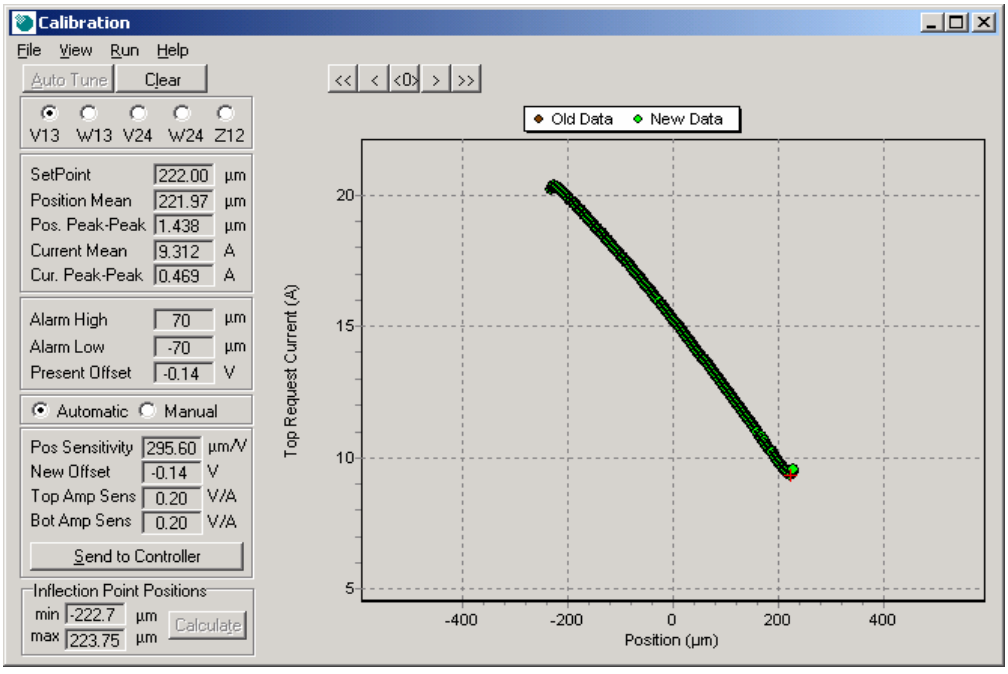

Fig. 10 MBCalibration Screen for Bump Test

Table 1 contains the voltage offsets from the bump tests. The uncertainty in these measurements is ± 0.01 V or less. This is equivalent to approximately 3 μm, about 1% of the radial clearance between the auxiliary bearings, or about 0.5 % of the radial clearance between the rotor laminates and the magnetic bearing poles

Table 1 Voltage Offsets from Bump Tests

Axis	Voltage Offset
V13	-0.14 V
W13	-0.72 V
V24	-0.04 V
W24	-0.77 V

Magnetic Bearing Proximity Probe Calibration

Proximity Probe Calibration (PPC) was performed by placing a digital indicator with accuracy ± .5 μm in contact with the shaft along the axis to be tested (Figure 11). The angle of the indicator was adjusted to 45° to coincide with a coordinate axis for the MBs. The perpendicularity of the indicator to the rotary axis was determined by using a precision indicator tip with a large planar contact area.

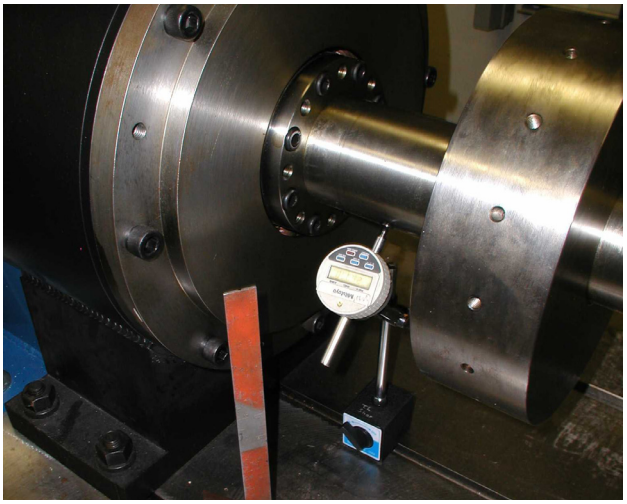

Fig. 11 Digital Indicator Setup

The error in angle between the magnetic bearing axis and the indicator axis could have been in as large as 8° without producing a significant impact on calibration. Eq. 1 displays the relationship between the actual motion and the detected motion depending on the angle error, θ.

$$\Delta x_{\text{actual}} = \Delta x_{\text{detected}} \cos\theta \tag{1}$$

A calculation follows which demonstrates the effect of an 8° error. The maximum actual position change was approximately 50 μm. In the calculation, it can be seen that the angle error produces an undetectable error in the indicator reading because the increment of the digital indicator reading is 1 μm. It should be noted that, while the angle error was unknown, it was substantially less than 8°.

$$\begin{aligned} \Delta x_{\text{detected}} &= \Delta x_{\text{actual}} / \cos\theta \\ &= 50 / \cos 8° \\ &= 50.49 \ \ \mu\text{m} \end{aligned} \tag{2}$$

Figures 12 through 15 contain the results of the PPC. The results appear to be extremely linear as correlation coefficients are 0.9998 or higher. Any irregularities could either be a slight non-linearity, or a result of the digital indicator precision. The results could likely be improved by using an indicator with a higher order of precision.

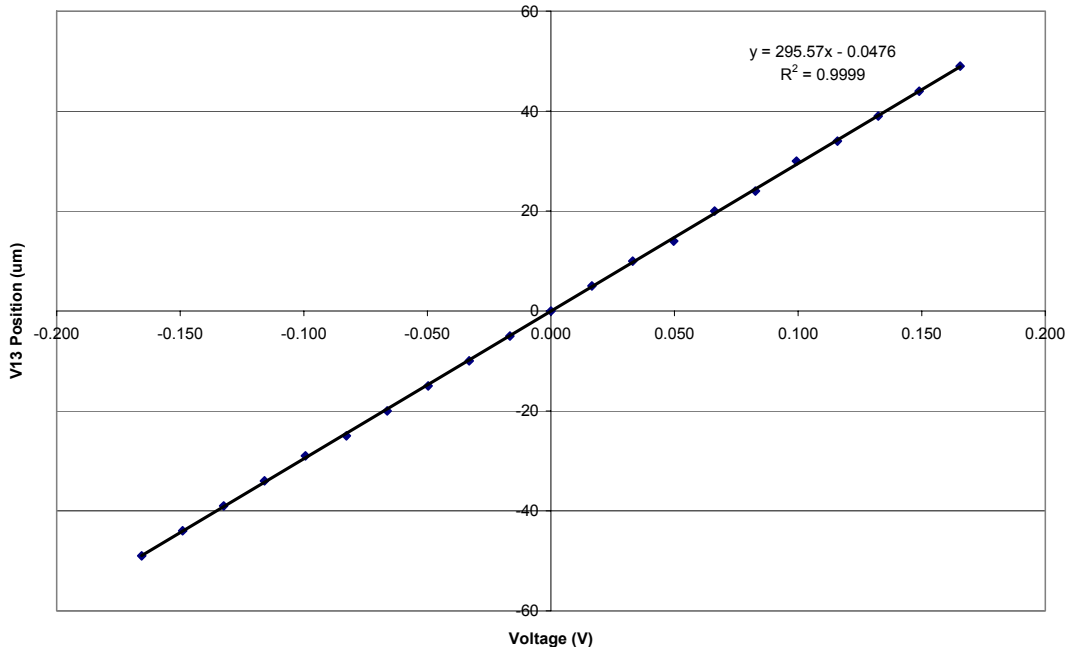

Fig. 12 V13 Axis Proximity Probe Calibration

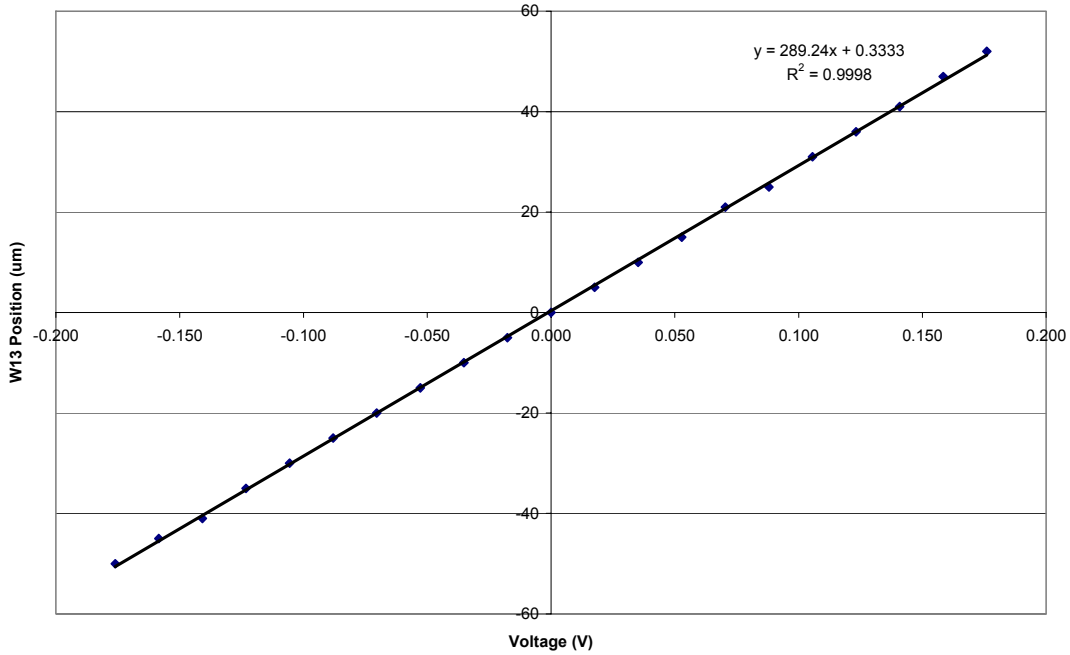

Fig. 13 W13 Axis Proximity Probe Calibration

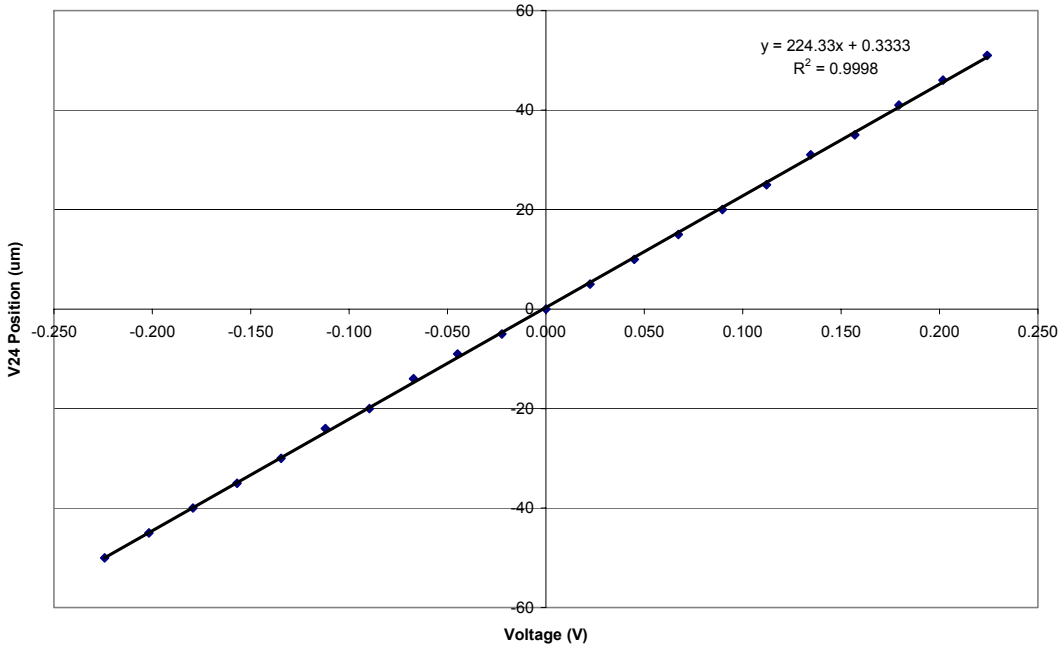

Fig. 14 V24 Axis Proximity Probe Calibration

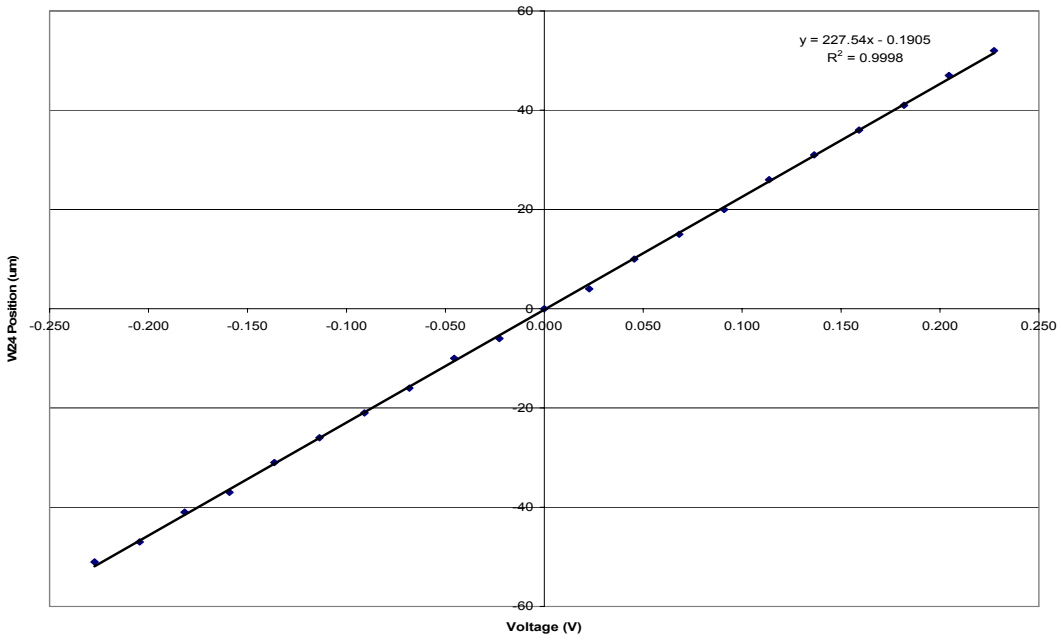

Fig. 15 W24 Axis Proximity Probe Calibration

The PPC coefficients (position sensitivity for each axis) are given in Table 2. The results are reasonable and very comparable to previous results obtained using a slightly different calibration method. Based on the precision of the digital indicator, the uncertainty in the coefficients is ± 1% (2 to 3 μm/V). Again, it is likely that a digital indicator with higher precision could reduce the uncertainties.

Table 2 Position Sensitivities

Axis	Position Sensitivities
V13	295.6 μm / V
W13	289.2 μm / V
V24	224.3 μm / V
W24	227.5 μm / V

MBScope Current-Position Formula

An accurate calibration of the current and position dependent magnetic bearing force model is required for the Current-Position FOSG Calibration (discussed in the *Fiber Optic Strain Gauge Calibration* section). One such formula is used in the MBScope software to produce theoretical force data. The MBScope formula can also be modified to create a more general form and implemented with data from the analog outputs of the MBResearch panel. The former is considered in this section.

The Controller Settings program in the MBScope software provides a single net force for each axis from data received through the serial port from the MBControl unit. Eq. 3 displays the Current-Position Formula used by this method.

$$F = C\left[\left(\frac{I_{top}}{2(g-x)}\right)^2 - \left(\frac{I_{bottom}}{2(g+x)}\right)^2\right] - F_0 \qquad (3)$$

The force F along a given axis is modeled as a function of the top current I_{top} and bottom current I_{bottom}, and rotor position x. In addition, two parameters must be determined and saved in the Controller Settings program. The effective gap g is a measure of the effective air gap between the rotor laminates and poles. Accurate calibration of this parameter is essential because if, for example, the parameter is set too low, the force result will be more sensitive to position changes and produce inaccurate results. The calibration factor C is the overall factor relating the current and position information to the force. Again, the accuracy of the formula depends on the accuracy of this coefficient; however, this fact is more intuitive and is not as easily overlooked. The tare force F_0 is useful in zeroing the force result for the static result of the current and position calculation. The tare force is not an accurate reflection of the rotor weight because the Current-Position Formula is only valid for a limited range. The tare force has no effect on the results that are related to relative changes in force, and as a result, the tare force will not be considered further.

The forces calculated using the Current-Position Formula are accessed through the Snapshots Tool in the MBScope software. This can provide a means for observing forces with relative ease. However, this approached had several drawbacks that prevented the use of the MBScope software for the calibration of the Current-Position Formula. The first problem is that there are only two parameters, g and C, that can be adjusted to calibrate each axis. Each axis has two poles that are neither identical nor operating about the same point (average current), and the force would be better modeled if each pole had an effective gap setting and a calibration factor. It can also be difficult and time consuming to synchronize the Labview VIs and the MBScope software. Finally, the data transfer rate for the MBScope serial connection only allows a single channel (one axis force) to be obtained at a high sampling frequency.

MBResearch Current-Postion Formula

The drawbacks of the MBScope formula prompted the uses of a modified Current-Position Formula with the analog outputs from the MBResearch panel. The

MBResearch panel connects to the MBControl unit and provides access to some of the signals that are used by the controller. Position, top current, and bottom current signals are available for each axis. Eq. 4 is the modified version of the Current-Position Formula from Eq. 3.

$$F = C_{top}\left(\frac{I_{top}}{2(g_{top} - x)}\right)^2 - C_{bottom}\left(\frac{I_{bottom}}{2(g_{bottom} + x)}\right)^2 - F_0 \quad (4)$$

Effective Air Gap

The effective gap parameters are calibrated first because the calibration factors depend on the gap parameters. A waveform was created in Labview with a frequency of 1Hz and an amplitude that corresponded to a rotor motion of 15 um. The waveform was injected into the analog inputs of the MBResearch panel. The inertial force generated by this motion was less than 0.1 N, and was therefore neglected. The data were analyzed using a Matlab FFT calculation. Eq. 5 is the calculation performed prior to the FFT. The position x is either added or subtracted depending on whether the calculation is for a top or bottom pole.

$$F_{uncalibrated} = \left(\frac{I}{2(g \pm x)}\right)^2 \quad (5)$$

The effective gap was adjusted for several iterations until a minimum FFT result was obtained at the excitation frequency. This calculation was repeated for larger amplitudes of up to 50 μm. The reasoning behind this method is that the actual oscillating force applied to the rotor was negligible, and the appropriate gap parameter would therefore be the one that minimized the FFT amplitude of the formula. Figure 16 displays the current, position, and force time traces as well as an FFT plot of the force for a non-minimizing effective gap value. These results demonstrate the possibility of producing

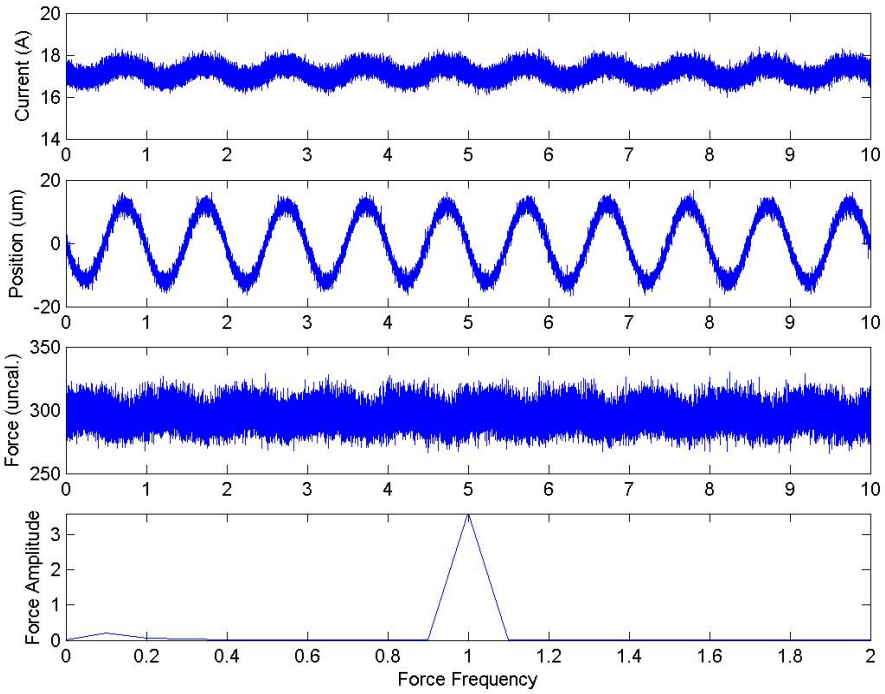

Fig. 16 Effective Gap Calibration with Non-Minimizing Value

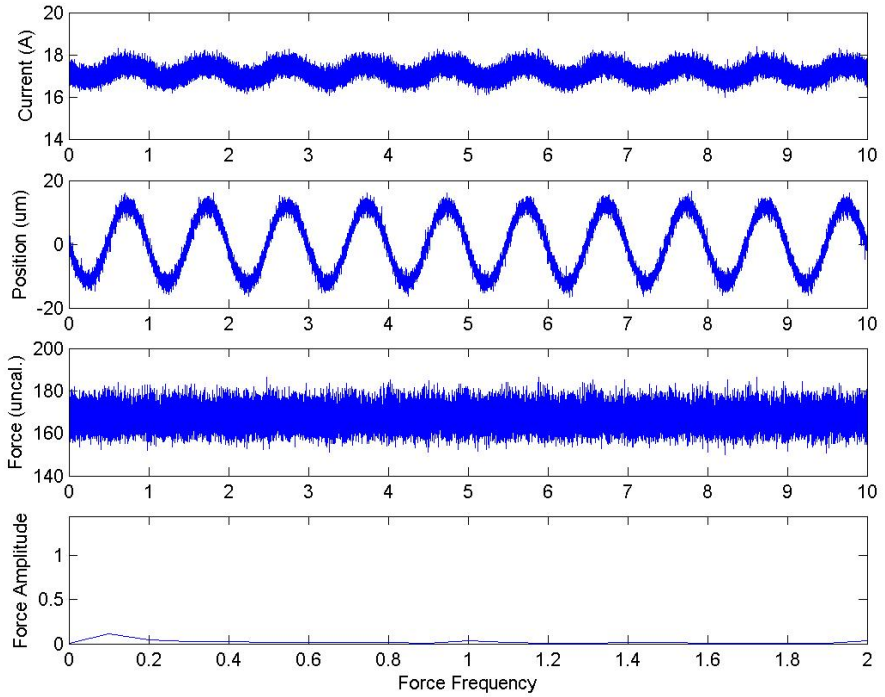

Fig. 17 Effective Gap Calibration with Minimizing Value

large erroneous force values by miscalibrating this parameter. Figure 17 displays the same information for a minimizing effective gap value. The time trace of the force does not contain noticeable variations at the excitation frequency, and this is also reflected the FFT plot.

Table 3 contains the effective gap parameters determined by the above method. The values for the top poles differ significantly from the bottom poles. This is an indication that sensitivity of the force to the position varies with the average current because the top poles have much higher average currents than the bottom poles. This difference is the first indication of a problem with the current and position dependent force model that will have a negative effect on the feasibility of using this method to calibrate. The uncertainty in the effective gap values is ± 5 μm based on the results from multiple tests. The accuracy of this calibration will have only a small effect on the accuracy of the Current-Position FOSG Calibration because the shaft motions from the center are very small.

Table 3 Effective Gap Parameters

Axis	g
V24 Bottom	272 um
V24 Top	664 um
W24 Bottom	252 um
W24 Top	705 um

Calibration Coefficient Ratio

The top and bottom calibration coefficients for the Modified Current-Position Formula cannot simultaneously be determined by applying a load to the rotor. Eq. 6 is a variation of the Modified Current-Position Formula. The ratio of the calibration coefficients can be determined by varying the top and bottom applied forces while maintaining the net force between them. This ratio is obtained by injecting current signals simultaneously into the opposing poles. The top and bottom poles are pulling against each other without causing the rotor position to change significantly.

$$F = C_{top}\left[\left(\frac{I_{top}}{2(g_{top}-x)}\right)^2 - \frac{C_{bottom}}{C_{top}}\left(\frac{I_{bottom}}{2(g_{bottom}+x)}\right)^2\right] - F_0 \qquad (6)$$

The MBControl module does not accept an injection of this nature while operating in the radial magnetic bearing mode. However, by changing the settings to the conical bearing mode, current can be injected simultaneous into the top and bottom poles by injecting a signal into the z-axis analog input on the MBResearch panel. Figure 18 is an example of a conical magnetic bearing.

Fig. 18 Conical Magnetic Bearing

The data is again acquired through the MBResearch panel. Separate, uncalibrated top and bottom forces are calculated as in Eq. 5. The bottom uncalibrated force is multiplied by the calibration coefficient ratio, and the top and bottom uncalibrated forces are subtracted, as shown in Eq. 7. FFT analysis of the net uncalibrated force is performed. The calibration coefficient ratio is iterated, and the correct calibration coefficient ratio minimizes the amplitude of the net uncalibrated force at the excitation frequency. This approach enforces the assumption that the net oscillatory force between top and bottom poles is negligible relative to the magnitude of the top and bottom oscillatory forces.

$$F_{net\ \ uncalibrated} = \left(\frac{I_{top}}{2\left(g_{top} - x\right)} \right)^2 - \frac{C_{bottom}}{C_{top}} \left(\frac{I_{bottom}}{2\left(g_{bottom} + x\right)} \right)^2 \tag{7}$$

The input signal to each axis was a post-filter current signal with amplitude of 1 A at a frequency of 1 Hz. This means that the MBControl module computes a response current and then adds the current indicated by the analog input. Figure 19 displays the net uncalibrated force and the FFT plot of the force amplitude for a non-minimizing ratio. Figure 20 displays the same information for the minimizing ratio.

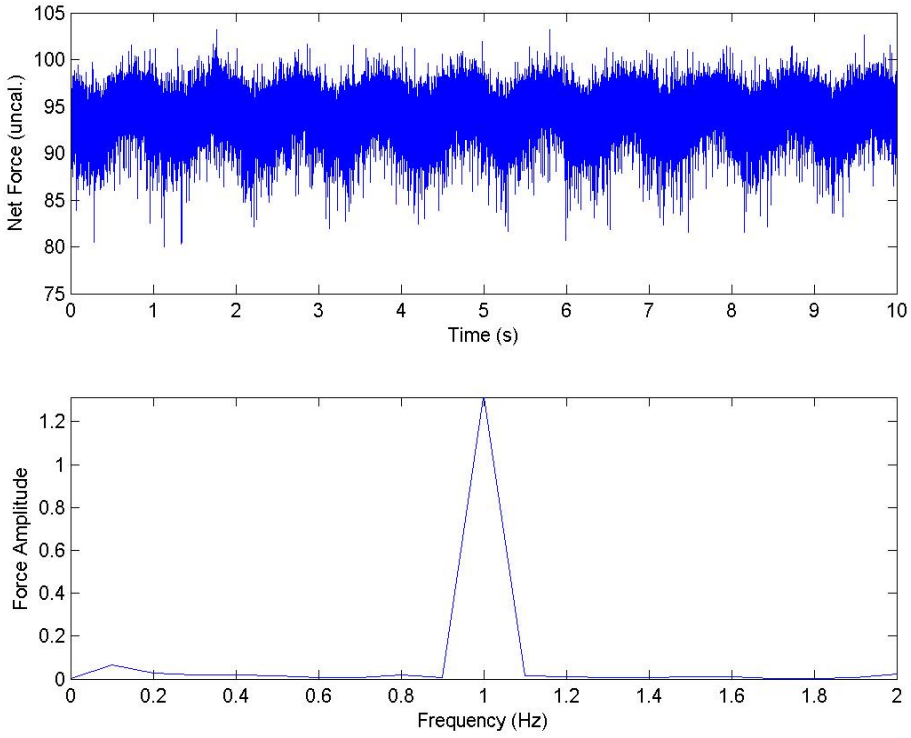

Fig. 19 Net Uncalibrate Force with Non-Minimizing Calibration Coefficient Ratio

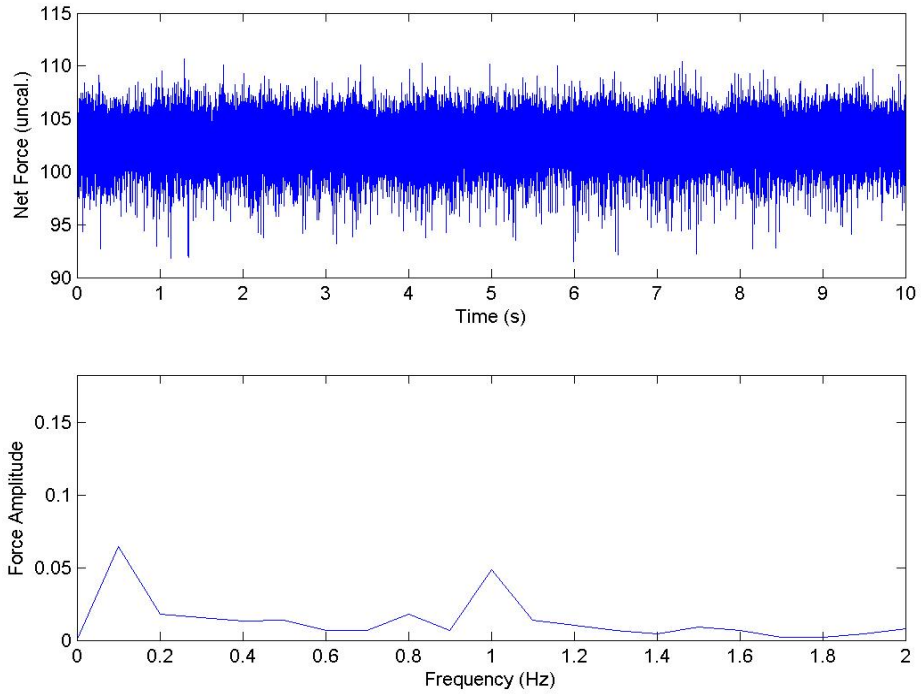

Fig. 20 Net Uncalibrated Force with Minimizing Calibration Coefficient Ratio

Table 4 contains the calibration coefficient ratios for the FOSG equipped axes. At first glance, the results seem unusual because one might expect the value to be closer to unity. However, the calibration coefficients are affected by the effective gap parameters. The effective gap parameters for the bottom poles are considerable less than those of the top poles; hence, the calibration coefficients are smaller for the bottom than for the top. The uncertainty in the ratios is $\pm$ 0.001 for the data that were analyzed. However, it will become apparent from following results that the resulting ratio would likely change for a different current signal amplitude.

Table 4 Calibration Coefficient Ratios

Axis	C Ratio
V24	.393
W24	.296

Calibration Coefficients

The final step in calibrating the parameters of the Modified Current-Position Formula is to apply an external load to the shaft and calculate the calibration coefficients. The external load was applied by hanging a weight in the center of the shaft. The uncertainty in the load applied to each axis is considered to be low relative to other uncertainties of the calibration process. More importantly, the application of the load is very repeatable. Accordingly, an improvement in the accuracy of the load applied to each axis would improve uncertainty in the calibration but not the repeatability. In other words, if the load applied to each axis were known with absolute certainty, it would not improve the repeatability of the calibration. The results of this calibration will help to clarify this issue.

The weight applied a force of 157 N to each axis. The post-filter current signals used in the previous section were injected. The net uncalibrated force was calculated according to Equation 3-5, and an average was taken. Next, the process was repeated without a load. Five tests, each with and without the load, were performed. The applied load of 157 N was divided by the average change in the net uncalibrated force to determine the calibration coefficients. The resulting calibration coefficients are displayed in Table 5. The standard deviation of the changes in the net uncalibrated force for the tests was approximately ±5% of the change. This translates into a standard deviation of the changes in the Modified Current-Position Model of ±8 N. Based on correspondence with Revolve Magnetic Bearings Inc., the uncertainty of the Current-Position Formula forces for a bearing with a load capacity of 3560 N is approximately ±10 N.

Table 5 Calibration Coefficients

Axis	C Values
V24	5.041 N mm^2 / A^2
W24	5.395 N mm^2 / A^2

To revisit the discussion of the accuracy of the applied force values, it is unlikely that applying a force in a more precise way would improve the repeatability of this calibration process. Further developments will reinforce the assertion that the applied load accuracy was sufficient for the scope of the present research. With the modified Current-Position Formula, the FOSGs can be calibrated based on the force calculation from the formula.

III. FIBER OPTIC STRAIN GAUGE CALIBRATION

The calibration of the FOSGs is dictated by several factors that affect the accuracy of the calibration. The FOSGs are affected by temperature changes, which typically occur at or below 1 Hz [11]. This requires that the applied calibration force must be dynamic and above 1 Hz. Additionally, the previous experiments [10] have demonstrated the accuracy of using a calibrated exciter, and the present research emphasizes the use of inertial forces of the rotor to calibrated the FOSGs. This approach would allow for field calibration of MBs in a machine without disassembly and is therefore of interest for practical applications.

Three calibration methods have been attempted and are described in this section. The Current-Position FOSG Calibration is accomplished by using the Current-Position Formula to calibrate the FOSGs. The Inertial FOSG Calibration uses a calculated force based on the acceleration of the rotor to calibrate the FOSGs. The Rotor Drop FOSG Calibration uses rotor weight or an external weight and the step changes in the FOSG readings that occur when the rotor delevitates to calibrate the FOSGs. The calibration results and a characterization of uncertainties are given for each method. The inertial calibration proves to be the most accurate and will be used in succeeding sections.

Current-Position FOSG Calibration

With a calibrated Current-Position Formula, the FOSGs can be calibrated by injecting the simultaneous post-filter current signal. This procedure was followed during the final steps of the Current-Position Formula calibration. Simultaneous injection causes the bearing poles to pull against one another without moving the rotor. The FOSGs detect the strain and the FOSG signals can be calibrated against the results of the Current-Position Formula.

Figure 21 is a plot of the data acquired for the Current-Position FOSG Calibration. The FOSG signals (1), the currents in the top poles (2), the currents in the bottom poles (3),

and the rotor position signals (4) are labeled. The signals are shown for both axes and two FOSGs. The figure shows that the FOSG signals and currents are all in phase, and the bearing is operating as intended. In addition, the rotor motion is seen to be at high frequencies and irrelevant for the calibration process.

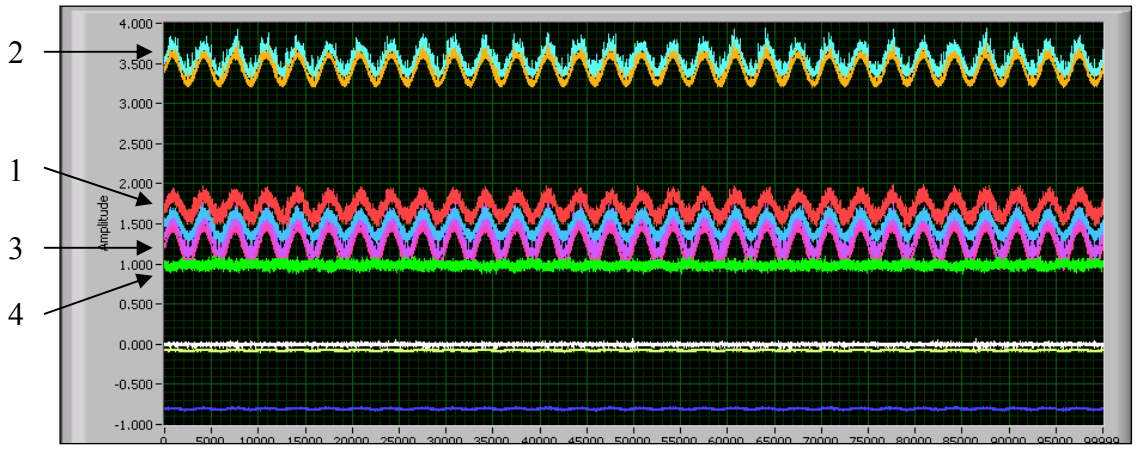

Fig. 21 Acquired Signals for Current-Position FOSG Calibration

With the acquired data, the forces in each pole are calculated using the Current-Position Formula, and an FFT is performed to obtain the force amplitudes. An FFT is also performed to obtain the amplitudes of the FOSG signals. The FOSG calibration coefficient is calculated by dividing the force amplitudes by their respective FOSG voltage signal amplitudes. Figure 22 displays the force FFT plot and the FOSG FFT plot. The plots suggest that the signal to noise ratios are acceptable. The FOSG plot shows larger noise levels at frequencies below 1 Hz, which agrees with previous experimental results [10]

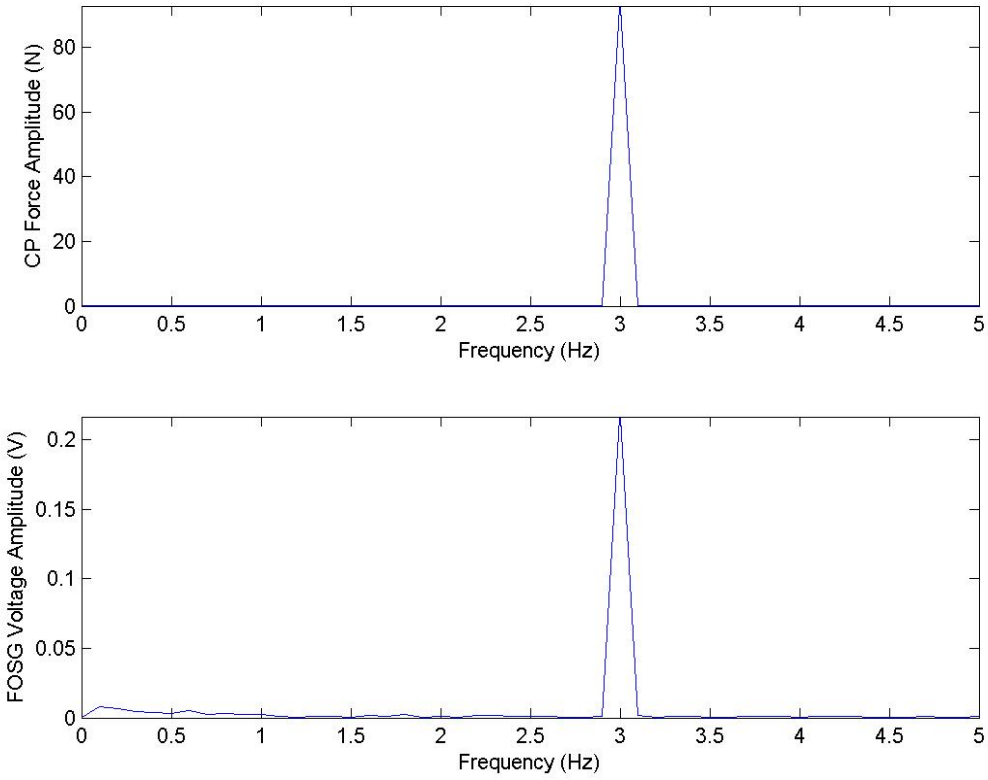

Fig. 22 Force and FOSG Voltage FFT Plots for 1.0 A Current Injection

Post-filter current injection signals had amplitudes from .2 A to 1.0 A with frequencies of 3 Hz and durations of 10 seconds. Figure 23 contains the results of the Current-Position FOSG Calibration for different current injections. Despite the excellent signal to noise ratios, the results varied considerably between the different current injections.

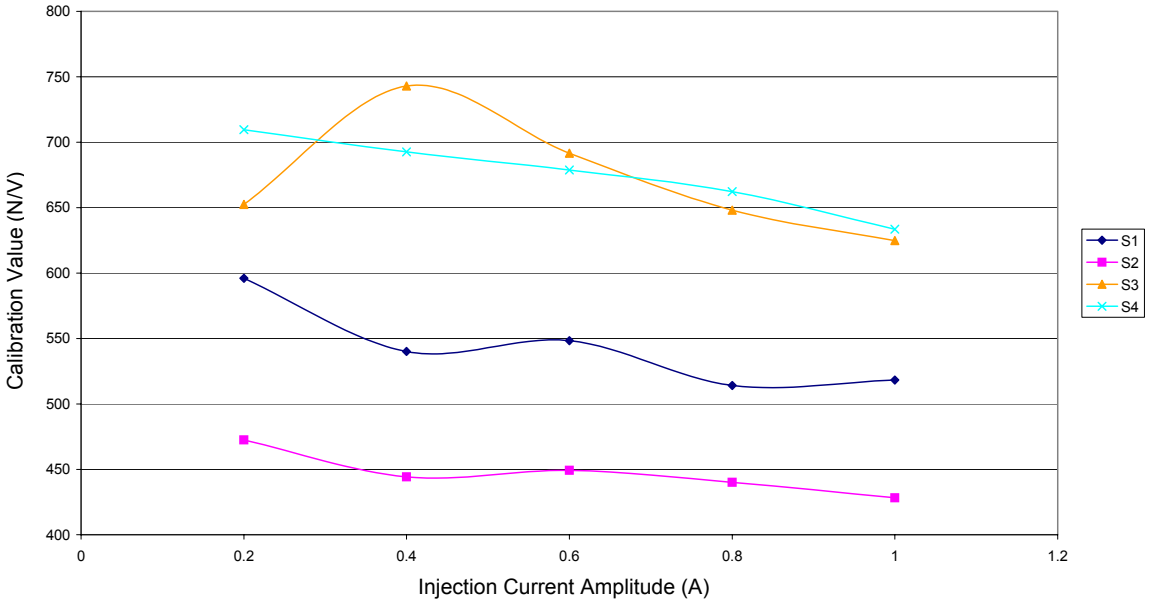

Fig. 23 Current-Position FOSG Calibration

At present, this result is best explained by the possibility that the coefficients for current and position dependent force models vary with the amplitude of the force. This suggestion is corroborated by results of other efforts in determining forces of MBs. Pottie [9] implemented a current and position dependent force model that involved mapping calibration coefficients for different force amplitudes. This outcome indicates that a specific set of parameters for the Current-Position Formula would only be valid for a small range of forces. Pottie experienced little success in using the mapping method for accurate measurements. Based on the results from the Current-Position FOSG Calibration, a strong argument cannot be made for the potential accuracy of this calibration method.

The Current-Position FOSG Calibration has several complications. The Current-Position Formula must be calibrated, which means any uncertainties in this calibration are transmitted to the Current-Position FOSG Calibration. The force values from the formula have low repeatability compared with the intended accuracy of the experiment. The parameters of the model and, as a result, the model itself depend on additional

factors such as the amplitude and frequency of the force. In its present form, the Current-Position FOSG Calibration can probably not produce uncertainties of less than 10 to 20% in the FOSGs calibration coefficients. For a typical test with dynamic forces on the order of one fourth load capacity, the uncertainties would translate to 2 to 5% of the load capacity. The later FOSG calibration methods will prove more successful.

Rotor Drop FOSG Calibration

The rotor drop calibration uses the step change in strain when the rotor delevitates to calibrate the FOSGs. Figure 24 displays the FOSG voltages during a rotor delivitation. The x-axis is sample number, and with a sampling rate of 10 kHz per channel, the interval shown is 1 second. In general, the FOSG calibration must be dynamic and at high enough frequencies to eliminate the effects of temperature drift. In this calibration, the split-second change in force between two static states can be considered, because the transition time between the two states is small enough to ignore temperature drift.

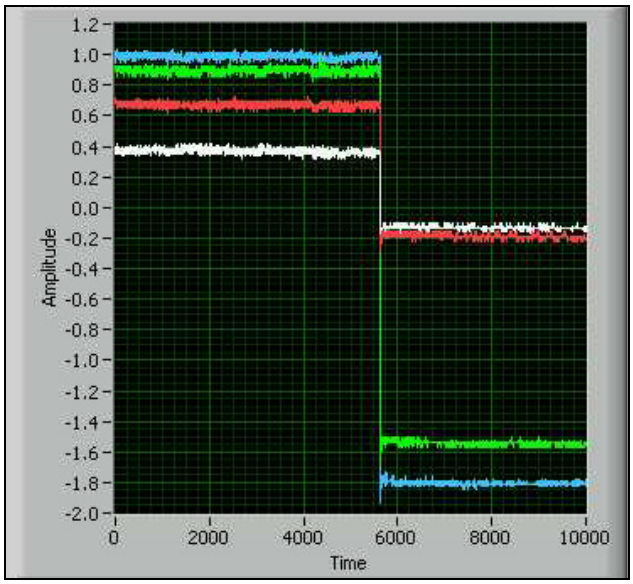

Fig. 24 FOSG Voltages during Rotor Delevitation

The first attempt was to calibrate the top strain gauges using the weight of the rotor. The bias currents in the bearings were set to zero. This meant that only the top poles were suspending the rotor. Once the top poles were calibrated, the bias currents were

increased and the bottom poles could be calibrated from the top poles. Despite acceptable repeatability, this attempt did not produce FOSG calibrations that agreed with previous results. The use of the rotor weight for calibration meant that data for the calibration was taken from a wide range of operating conditions. The calibration could also be affected by either a deadband or a nonlinearity at beginning of the force vs. FOSG voltage curve.

Figure 25 displays an example of a nonlinear force vs. FOSG voltage curve that would be detrimental to the present calibration. However, modifying the calibration method to utilize a smaller linear region allows a successful calibration despite possible initial nonlinearities. The slope of the testing region is represented by *s*, and the intercept for the region is given by *b*.

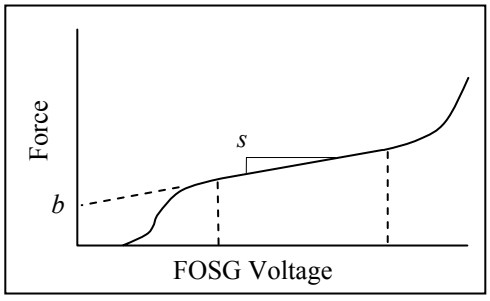

Fig. 25 Force-FOSG Voltage Model for Rotor Drop Calibration

The equation describing this model in the testing region follows. The force *F* is a function of FOSG voltage *V*.

$$F = sV + b \tag{8}$$

Eq. 8 is a summation of the forces along one of the axes. The rotor weight *W* is scaled by position of the center of gravity l_{cg} relative to the length of the rotor *l*. The weight is

then multiplied by the cosine of the angle θ, where θ is the angle of the axis from vertical direction.

$$\left(s_{top}V_{top} + b_{top}\right) - \left(s_{bottom}V_{bottom} + b_{bottom}\right) - \frac{Wl_{cg}}{l}\cos\theta = 0 \tag{9}$$

Placing a weight on the rotor w equidistant from each bearing modifies Eq. 9 as follows.

$$\left(s_{top}V_{top} + b_{top}\right) - \left(s_{bottom}V_{bottom} + b_{bottom}\right) - \left(\frac{Wl_{cg}}{l} + \tfrac{1}{2}w\right)\cos\theta = 0 \tag{10}$$

Subtracting Eq. 10 from Eq. 9 and rearranging creates the following equation, which can be calibrated.

$$\Delta V_{top} = \frac{s_{bottom}}{s_{top}}\Delta V_{bottom} + \frac{w\cos\theta}{2s_{top}} \tag{11}$$

The ratio of bottom to top slope is determined by varying the bias current of the MB about the normal bias current and plotting the top FOSG voltage change at delivitation vs. the bottom FOSG voltage change. The top slope was determined by hanging a weight at the center of the rotor, varying the bias current, and again plotting the top vs. bottom FOSG voltage change. The change in the intercept of the linear fit from the unloaded to the load plot Δb is equal to the constant term of Eq. 11. Eq. 12 relates the top slope to the applied weight w, and the intercept change Δb.

$$s_{top} = \frac{w\cos\theta}{2\Delta b} \tag{12}$$

Figure 26 displays the results of the calibration for the S1 and S3 FOSGs, and Figure 27 displays the results for S2 and S4. The uncertainties shown are 99.5% confidence intervals for the 30 repetitions at each point.

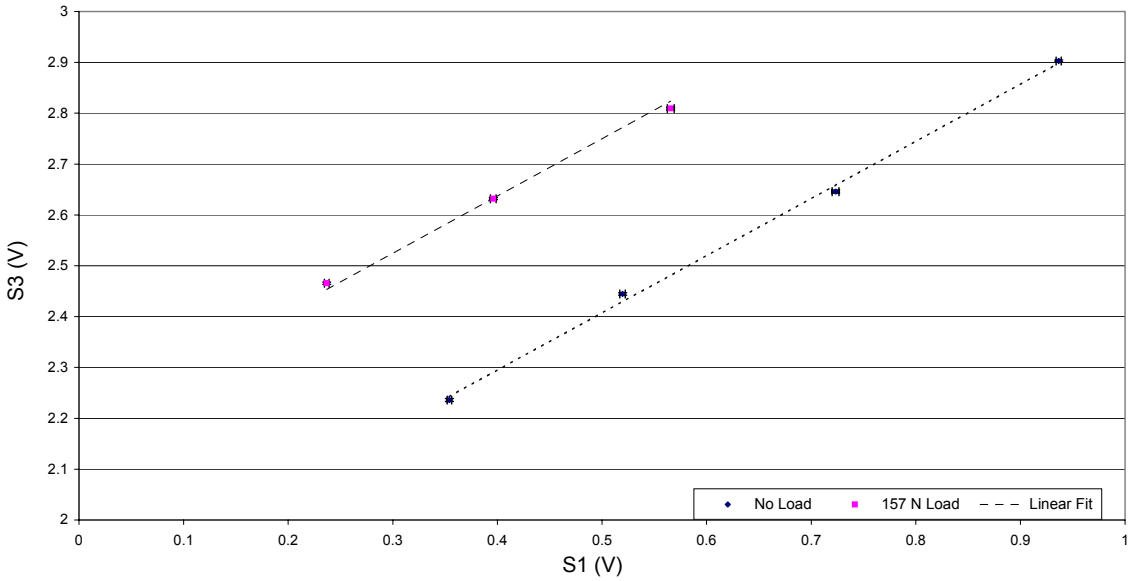

Fig. 26 S1 and S3 Calibration Results for Rotor Drop FOSG Calibration

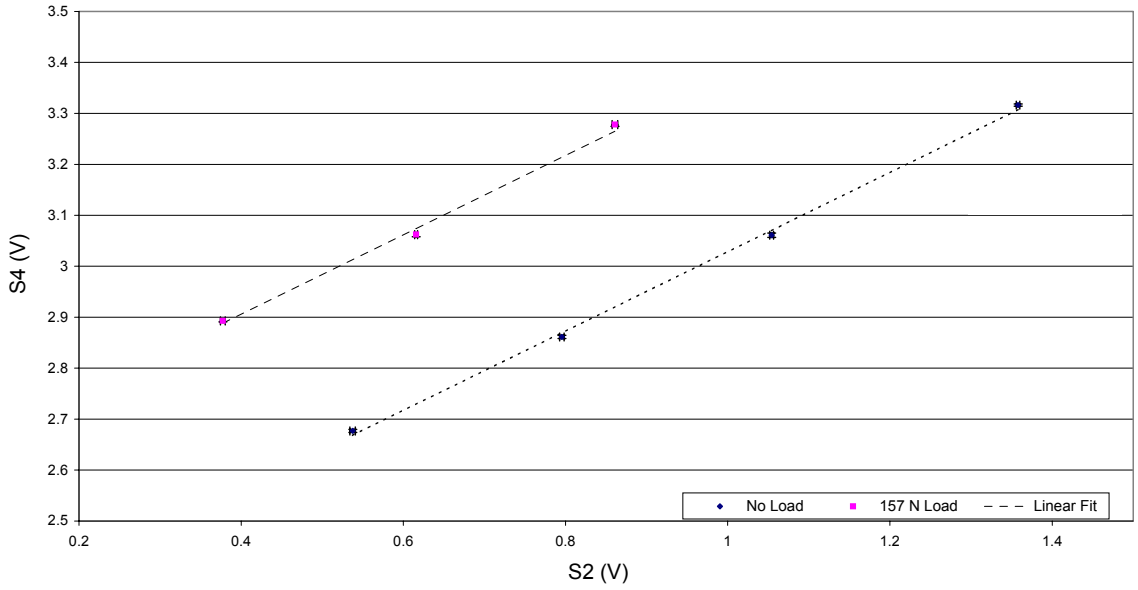

Fig. 27 S2 and S4 Calibration Results for Rotor Drop FOSG Calibration

The Rotor Drop FOSG Calibration results are given in Table 6. These results have excellent repeatability. The calibration coefficients are on the same order as the previous values, but they are significantly lower. The source errors in these coefficients is unclear; however, previous results with a calibrated exciter suggest that they should be higher [10] [11]. The low strain levels and elastic properties of the poles produce the expectation that the force vs. FOSG voltage change functions would be more linear, and, accordingly, the nonlinearity consideration would be unnecessary. The mechanism causing this apparent nonlinearity has not been identified, making the results somewhat suspect. In addition, the modification to the Rotor Drop FOSG Calibration required the use of an external load. This approach is undesirable for field applications. Consequently, the Rotor Drop FOSG Calibration has not been used in later testing.

Table 6 Rotor Drop FOSG Calibration Results

Axis	Cal. Value (N/V)
S1	515.9
S2	354.8
S3	457.7
S4	455.1

Inertial FOSG Calibration Background

The Inertial FOSG Calibration seeks to calibrate the FOSGs from the force required to accelerate the rotor. Forces to accelerate the rotor are produced by injecting a sinusoidal waveform into the MBResearch panel. The force produced by the waveform controls the rotor position and causes the rotor to oscillate. The first attempt was to shake only rotor end where the MB was equipped with FOSGs and calibrate from a rotational equation of motion. However, it soon became apparent that the motion at the other end of the rotor was unpredictable and would create a significant impact on the calibration. As a result, the data acquisition system was upgraded to provide 2 additional analog outputs and 8 additional simultaneously sampled analog inputs. This upgrade included the 6036E NI data acquisition PCI card and another external SC2040 card. The rotor

could now be translated without rotation by moving the rotor ends in phase along parallel radial axes. An additional benefit of this method is that the mass of the rotor and its center of gravity must be known instead of the mass moment of inertia.

Preliminary Results of the Inertial FOSG Calibration

This first attempts at the Inertial FOSG Calibration achieved limited success. However, these efforts provide insight that eventually led to the development of an accurate FOSG calibration method. The rotor was translated vertically at various frequencies to generate different magnitudes of inertial forces. Initially, the FOSG calibration was assumed to have vertical and horizontal symmetry, and the vertical direction was selected because the vertical support structure was stiffer and resulted in smaller MB housing motion. Eq. 13 defines the radial rotor position as a function of time. Equation 13 is the physical model initially used for calibration.

$$x(t) = X_0 \sin(\omega t) \tag{13}$$

$$F(t) = -\frac{ml_{cg}}{l} X_0 \omega^2 \sin(\omega t) \tag{14}$$

F is the magnitude of the net force applied at the FOSG equipped MB. The rotor mass m is multiplied by the distance l_{cg} measured from the bearing without FOSGs to the center of gravity and divided by the length l between the bearings. The position amplitude of the shake is X_0, and ω is the frequency of excitation. Eq. 14 is obtained by applying Newton's Law with the acceleration obtained as the second derivative of position.

Accelerometers were used to compensate for the motion of the bearings. Initially, the accelerometers had a large frequency range and low sensitivity. This characteristic, along with the necessity of a detectable force amplitude, required the excitation frequency to be a minimum of 30 Hz. An algorithm was developed that adjusted the

injection phases and amplitudes to obtain the desired rotor translation. For higher frequencies, the ends of the rotor would not remain in phase. Due to the translation repeatability decrease, the maximum frequency was limited to 65 Hz.

The excitation frequencies ranged from 30 to 65 Hz in increments of 5 Hz. The signals were injected for 14 seconds. The first 3 seconds and the last second of data were discarded. The remaining 10 seconds of strain and position data was analyzed using the Labview *Extract Single Tone Information* virtual instrument. This procedure was repeated 10 times at each frequency for uncertainty analysis. Figure 28 displays the strain amplitudes as a function of frequency for FOSGs S1 and S2. Uncertainty bars are included in the figure. Figure 29 contains the position amplitudes for the axes V13, W13, V24, and W24 as a function of frequency.

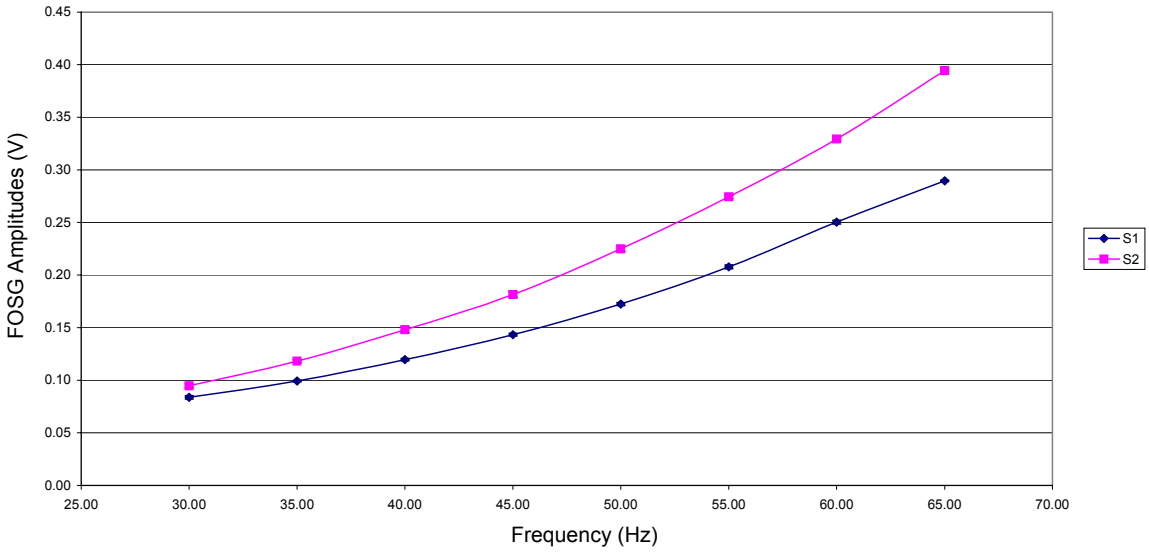

Fig. 28 FOSG Amplitudes for Inertial FOSG Calibration

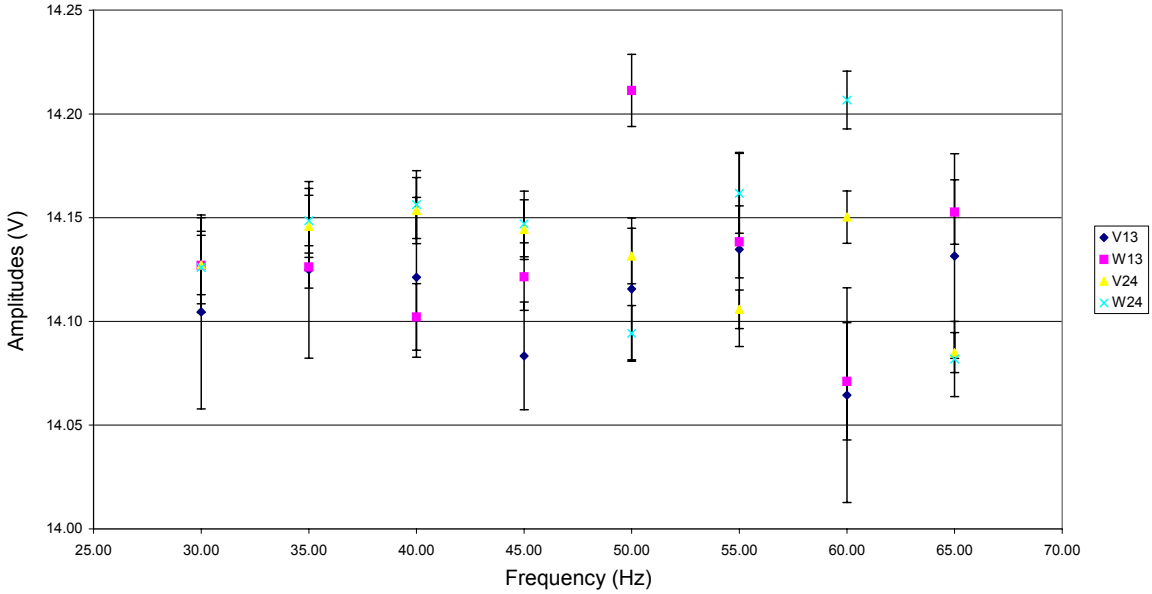

Fig. 29 Position Amplitudes for Inertial FOSG Calibration

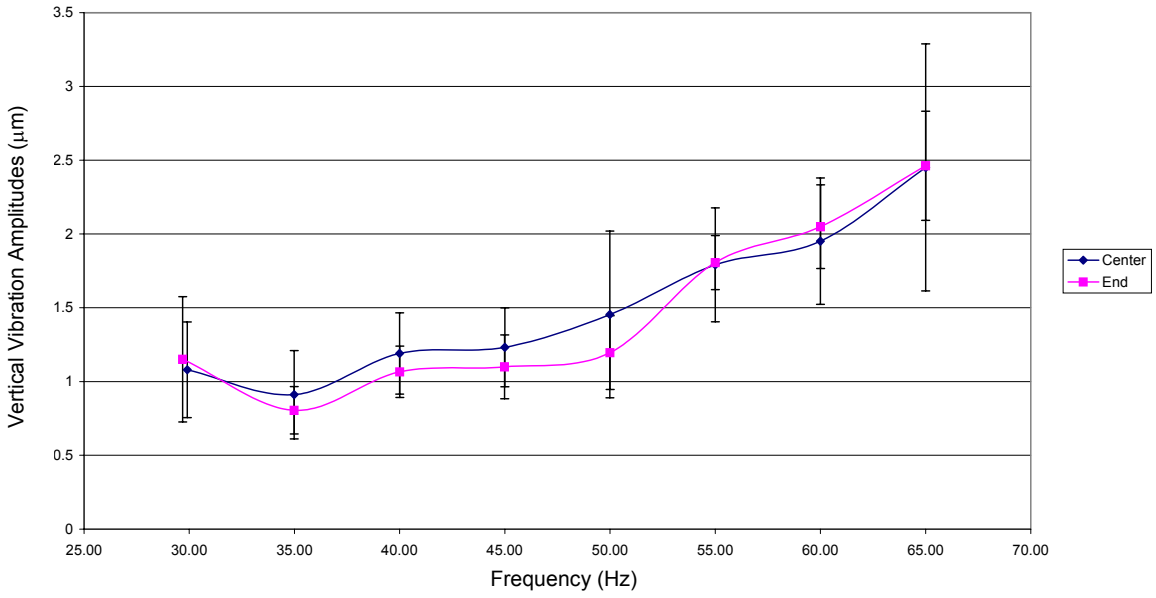

Fig. 30 Bearing Position Amplitudes for Inertial FOSG Calibration

The accelerations were converted to position changes using the excitation frequency. Figure 30 displays motion of the bearings as detected by the accelerometers. The accelerometer measurements were not nearly as repeatable as the position and FOSG measurements. These results were added to the measurements of the proximity probes to obtain the absolute rotor position amplitudes.

The change in force is assumed to cause a proportional change in the strain detected by the FOSGs given by Eq. 15. By computing the FFT amplitudes of the strain voltage signals V and the rotor absolute position $\widetilde{X}_0$, Eq. 14 and Eq. 16 can be solved for the FOSG calibration coefficient.. This calibration differs from the previous FOSG calibrations, because the strain of one pole is assumed to be a repeatable representation of the net force acting on the rotor along the axis of that pole. The calibration coefficients for this method can be loosely compared to those of the previous methods by dividing the present coefficients by 2. The controller for the MBs applies a force to the rotor by increasing the current in one pole and decreasing the current in the opposite pole by the same amount. The net force is roughly twice the magnitude of the force change at either pole.

$$F = kV \tag{15}$$

$$k = \frac{ml_{cg}}{l}\frac{\widetilde{X}_0\omega^2}{V} \tag{16}$$

Figures 31 and 32 plot the results of the calibration with and without considering the movement of the bearings. These results are clearly problematic because the calibration coefficients appear to change with frequency. The coefficients are expected to be constant and the assumptions of the Inertial FOSG Calibration must be more closely examined.

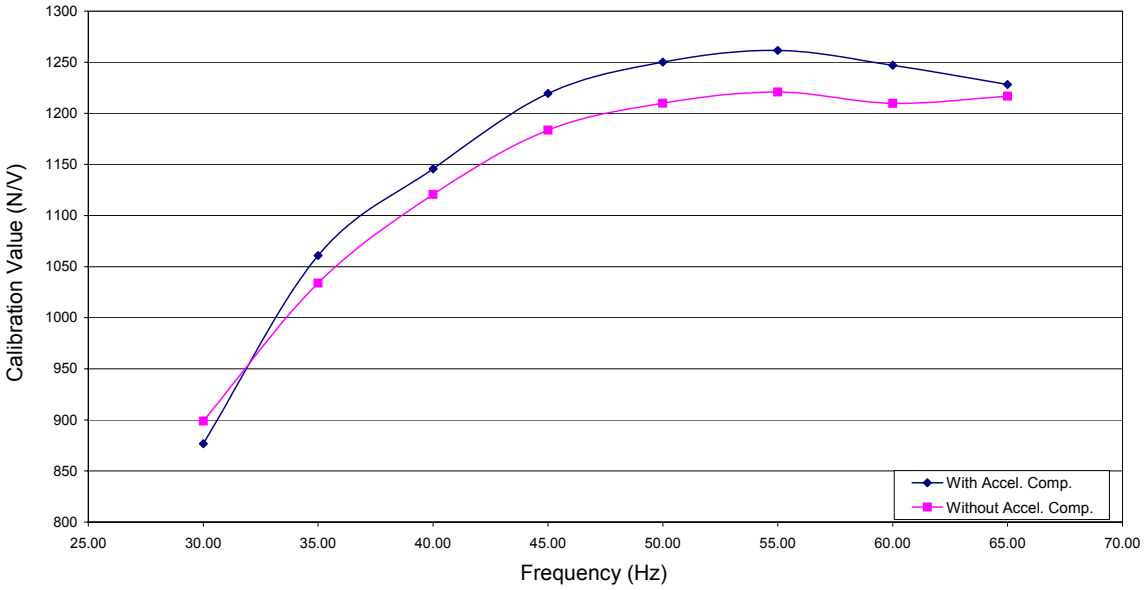

Fig. 31 S1 Calibration without Position Compensation

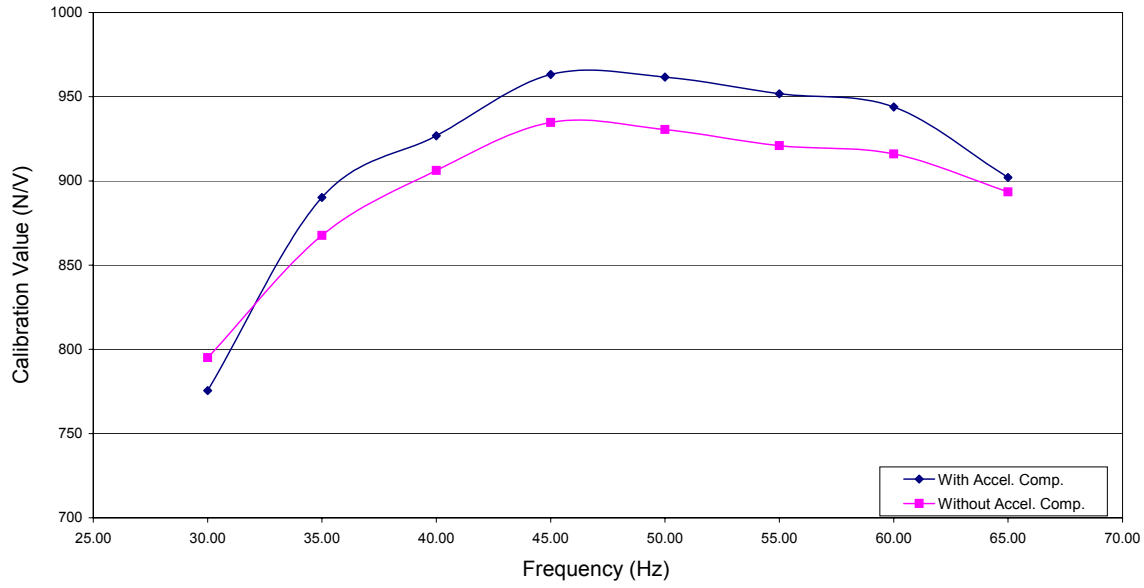

Fig. 32 S2 Calibration without Position Compensation

One possible source of error can be observed in Figure 28. As the excitation frequency goes to zero, the FOSG voltage amplitudes appear to approach non-zero values. This

suggests that the FOSG voltage depends not only on the force applied to the rotor, but also on the position of the rotor. Subsequent testing showed that translating the rotor at low frequencies generates substantial amounts of strain despite the fact that inertial forces are negligible. However, this position-dependent FOSG voltage is in phase with the forces and independent of frequency, allowing the position-dependent FOSG voltage to be subtracted prior to the calibration coefficient determination. Figures 33 and 34 display calibration results in which the position-dependent FOSG voltage has been subtracted from the test data.

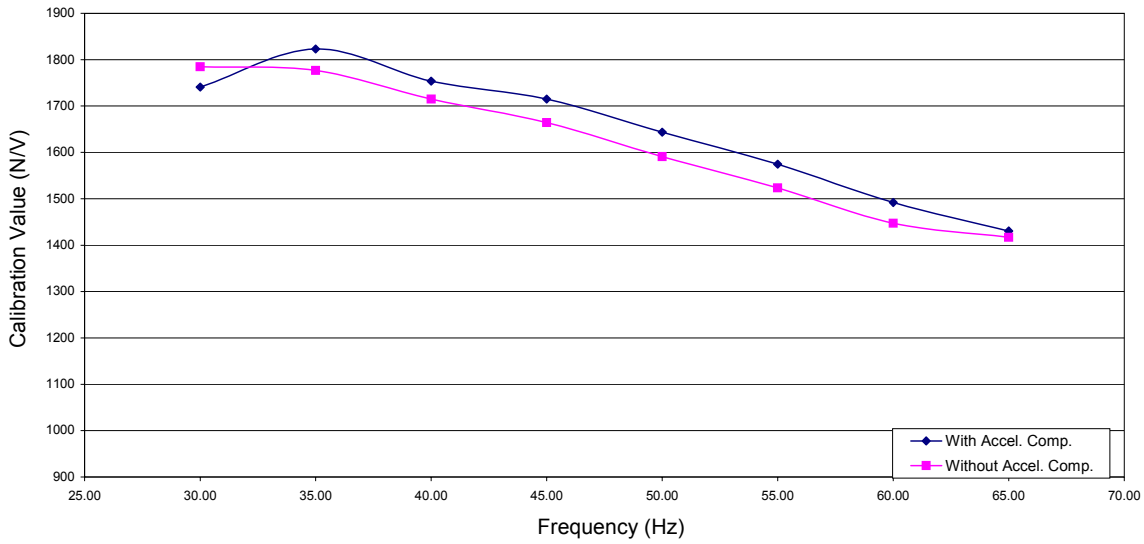

Fig. 33 S1 Calibration with Position Compensation

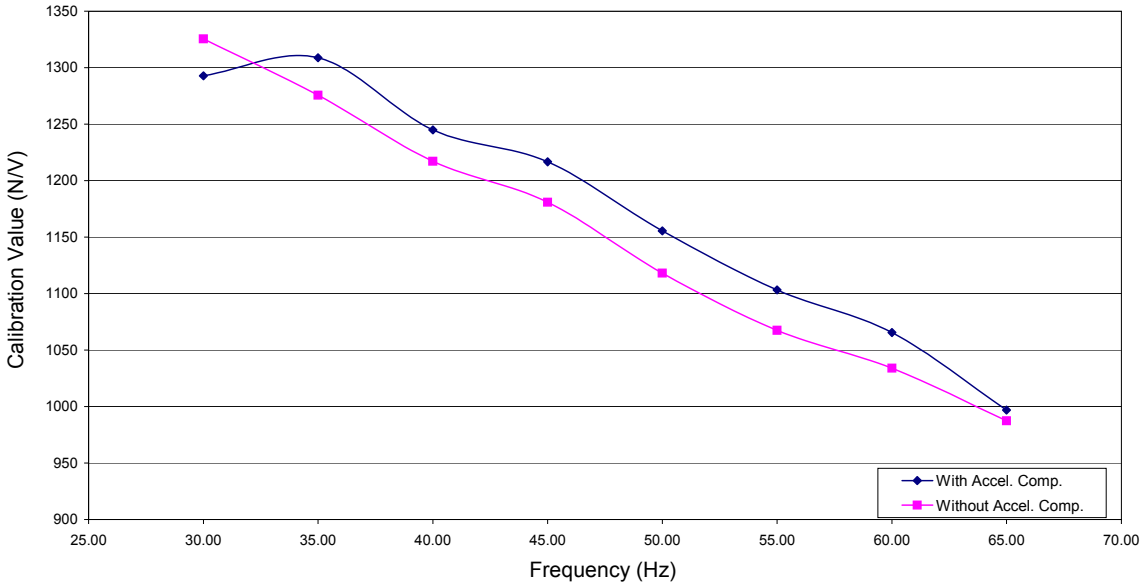

Fig. 34 S2 Calibration with Position Compensation

The calibration results are still unconvincing. However, the linearity of the plots has improved suggesting that the position-dependent FOSG voltage has been successfully removed. The assumptions must now be examined further. Other source of error could arise from the rigid rotor assumption or uncertainties in the accelerometer measurements. The results of the Inertial FOSG Calibration appear somewhat promising. However, the models and assumptions should be further evaluated to determine sources of error.

The Modified Inertial FOSG Calibration

The preliminary attempts at an Inertial FOSG Calibration were unsuccessful because the data reduction did not produce a clear consistent calibration. The inconsistency suggests that the model used for calibration was inadequate. A careful examination of the assumptions used in modeling reveals the errors that can be correct to improve the model and the calibration method. The most significant assumption of the model is the rigid rotor assumption. A detailed analysis of this assumption follows.

To examine the accuracy of the rigid rotor model, an assumed mode model was developed for the rotor. The rotor shapes were determined at the maximum amplitudes occurring during calibration. Figure 35 shows that the rotor undergoes considerable deformation despite the fact that the frequencies are well below the first bending mode of the rotor. The MB locations are marked, and the amplitudes at the MBs are all 20 μm, which is the calibration shake amplitude.

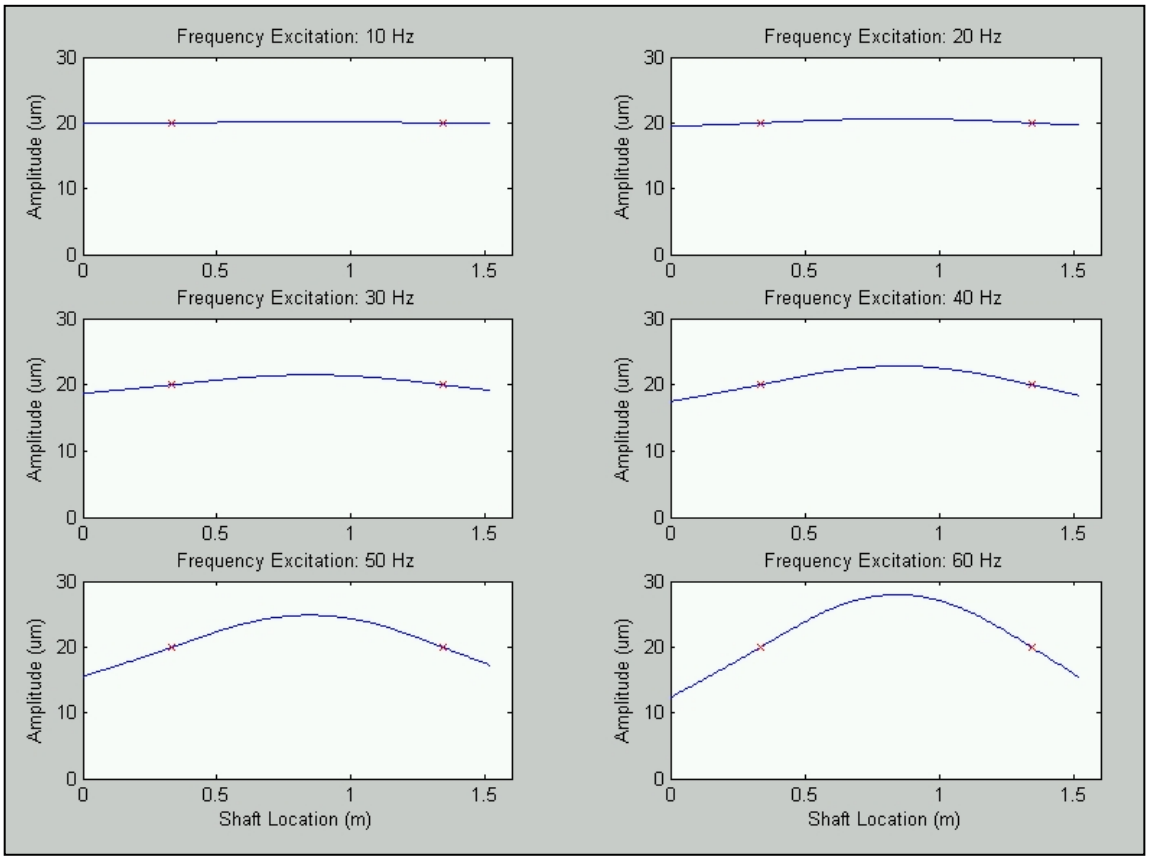

Fig. 35 Assumed Mode Rotor Shapes for 10 to 60 Hz Translation

The assumed mode model was validated by placing an accelerometer at the center of the rotor and injecting a calibration waveform. Figure 36 displays the position amplitude of the rotor at either end, obtained from the proximity probe measurements, and at the center, from the accelerometer.

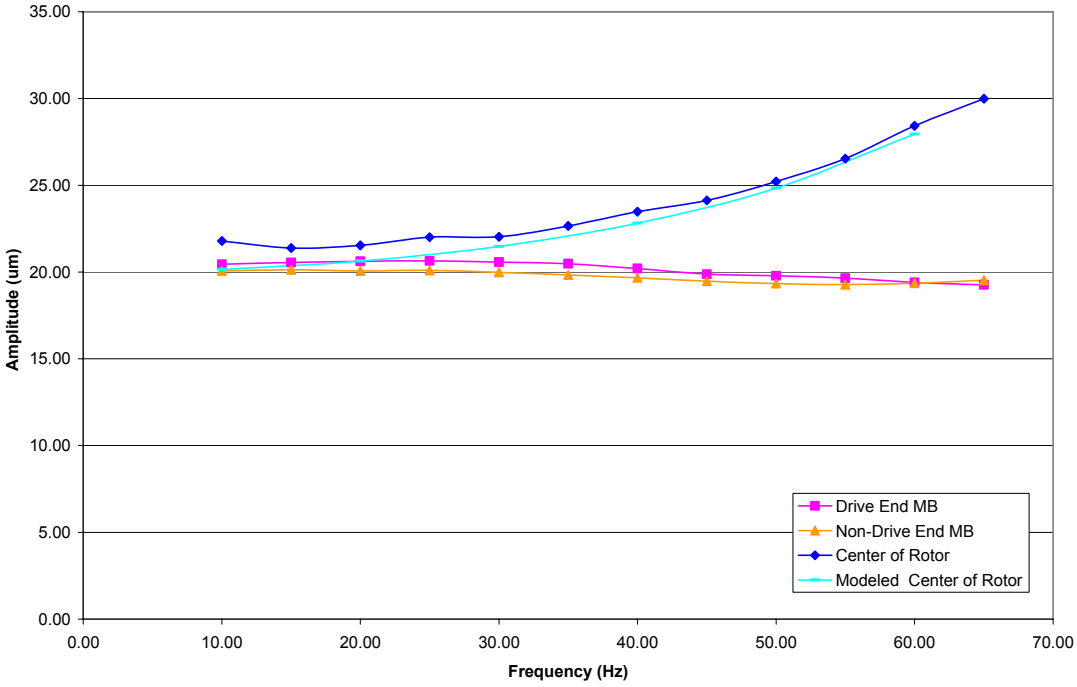

Fig. 36 Rotor Amplitudes from Experiment and Model

Agreement with the assumed mode model, particularly at high frequencies confirmed the need for an improved rotor model. A finite element model would be preferable to an assumed mode model, and the model was developed in XLTRC^2. It is displayed in the geoplot (Figure 37). A flexible rotor is considered with forces acting at the center of each of the rotor laminates (stations 9 and 23). An effective coupling mass is included, but stiffness from the coupling is neglected. The transfer functions of the MBs are not considered in the model for the following reason. Signals are injected into the MBControl module and iterated until the desired position response of the rotor is obtained. The location of the applied force is also considered to be the location of the proximity probes. The model uses the absolute position measurements to calculate forces. These forces are then converted into a correction factor used to calibrate the FOSGs.

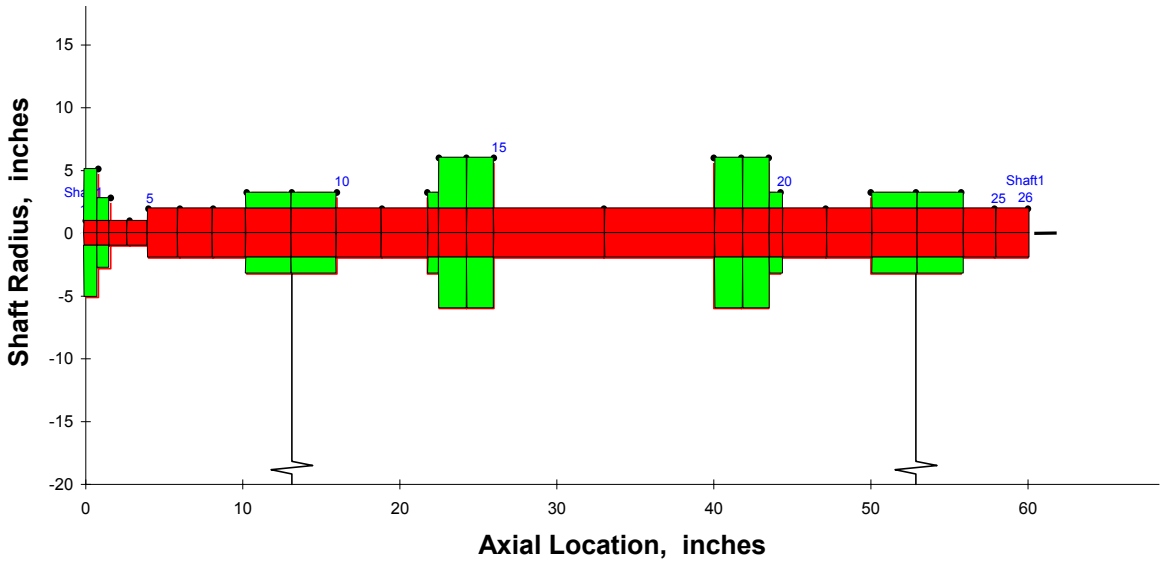

Fig. 37 XLTRC^2 Model of Rotor

Improvements were also made to the MB housing motion measurements. PCB seismic accelerometers are used to measure the low frequency (200 Hz or less) and low amplitude vibrations. They can detect as little as 1 micro-g and are calibrated for as low as .1 Hz. The data from the accelerometers is combined with the data from the proximity probes to determine the motion of the rotor relative to a fixed reference frame. These new accelerometers are considerably better than previous accelerometers. Figure 38 displays the MB position amplitudes obtained from the accelerometer measurements. Note that uncertainties are considerably lower and calibration frequencies as low as 10 to 15 Hz are possible.

Finally, the assumption of horizontal and vertical FOSG calibration symmetry was dropped. The details of the calibration coefficient determination are included in the following section. The physical mechanism causing the asymmetry is unclear, particularly since the precise geometry of the MB prevents effects typically associated with misalignment. However, conventional strain gauges routinely exhibit asymmetry and the matter is not considered further.

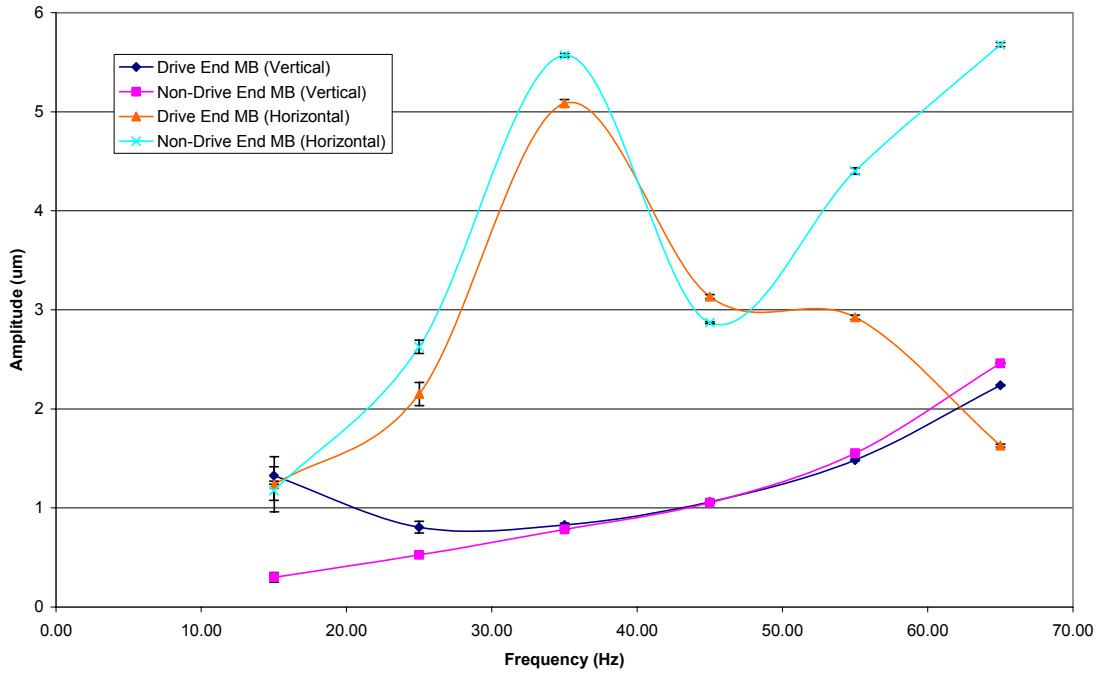

Fig. 38 Magnetic Bearing Motion during FOSG Calibration

These modifications to the Inertial FOSG Calibration considerably improved results. The flexible rotor model is by far the most important improvement. The following section shows that this improvement results in calibration coefficients that are independent of frequency. The accelerometer improvements have a smaller effect on the calibration, but the dramatic reduction in uncertainty increases the confidence in the position measurements of the rotor and the resulting calibration.

Inertial FOSG Calibration Method (IFCM)

The *IFCM: Testing Phase* section outlines the procedures for obtaining accurate calibration results using the Inertial FOSG Calibration Method. An explanation of the Labview testing program is also included. The *IFCM: Data Reduction* translates the data from the test into an accurate calibration for the FOSGs. Assumed mode and finite element rotor models are explained and the calibration matrix is determined. The *IFCM: Uncertainty and Discrepancies* section contains uncertainty results and a discussion of the discrepancy between the vertical and horizontal calibrations.

IFCM: Testing Phase

A Labview program has been designed to generate waveforms, create analog output signals, acquire data from analog inputs, and perform Fourier analysis on the data. The recent addition of another internal DAQ board and an external signal conditioning board greatly expanded the capabilities of the DAQ system. It also created some difficulties associated with timing the outputs and inputs. These difficulties will not be discussed in detail, but the general approach is to designate one board as a slave and use the same trigger signal for the analog inputs and outputs on both boards.

The Labview program loads two sets of parameters from a text file. The desired signal amplitudes and phases are loaded and used as target settings. It is important to produce extremely consistent position amplitudes and phases because of the assumptions used in deriving a calibration, which follows. Initial values for the injection signals are also loaded. The program uses the initial values to generate the waveforms and produce the analog output. The data from the proximity probes, accelerometers, and the FOSG SCU are obtained through the analog input channels. A built-in Labview VI called *Extract Single Tone Information* is used to determine the peak amplitudes and respective phases of all the signals within a specified frequency range. The position data are multiplied by the proximity probe calibration coefficients. Figure 39 demonstrates the process by which the initial values are adjusted to produce the desired amplitudes and phases. The measured positions $X_{measured}$ are subtracted from the desired positions X_{target} (complex vector subtraction) to obtain a position correction vector $X_{correction}$. The injection correction vector $V_{correction}$ is produced by rotating and scaling the position correction vector. The injection correction vector is added to the previous injection vector $V_{previous}$ to obtain the new injection V_{new}.

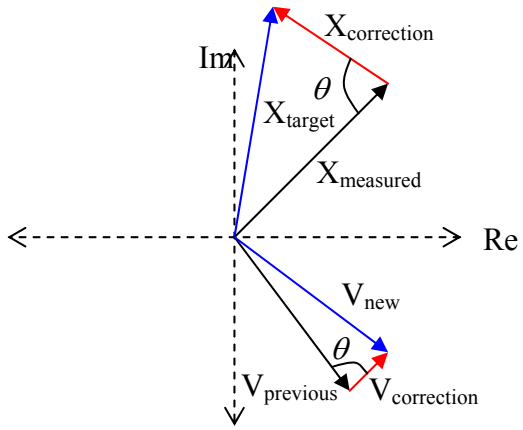

Fig. 39 Injection Waveform Iteration Process

This method drives the response to rapidly achieve the desired characteristics. The injection starts at the minimum injection voltage, or lowest rotor position. By starting at a point where the dynamic response has zero velocity, the transient is relatively small, and steady state is achieved quickly.

The Labview program continues to iterate the above process until the resulting waveform characteristics fall within specified bounds. The Fourier analysis results from the acceptable test are saved, and the iteration continues until 10 acceptable tests are produced. If the specifications for the amplitude error and phase error are reasonable, the majority of the subsequent tests are acceptable. The program then proceeds to the next frequency and repeats the process. The amplitudes can be controlled to less than .05 μm or .002 mils, and the phases can be controlled to less than .5°. This may sound unreasonably small, but the standard deviations from the repeated tests are around .02 μm and .2° for the amplitudes and phases respectively. This method for injecting waveforms provides significantly better control than previous methods. It is also faster because no user input is required during the calibration process.

The injected frequencies are 3 Hz and 10 through 65 Hz in increments of 5 Hz. 10 acceptable tests are taken at each frequency. The amplitudes are 20 μm and the orientation is typically vertical for the first set of frequencies and horizontal for the second, although this can be reversed. The measured frequencies, amplitudes and phases are saved to a text file for each accepted test. The results are then imported to an Excel spreadsheet for the data reduction.

IFCM: Data Reduction

The data are loaded into a spreadsheet, and the average and standard deviation are determined for each frequency. Next, several modifications are made to the data. The phase of the strain signals is shifted to account for the SCU delay of approximately 1 ms. The proximity probe measurements are transformed into vertical and horizontal axes. The accelerometer measurements are converted into displacement measurements and combined with the proximity probe measurements (complex vector addition) to obtain the absolute rotor displacement.

The next step is to modify the FOSGs measurements to account for the position related strain. The FOSG voltages respond to changes in the strain of the magnetic bearing cores. This means that strain is detected not only when the net force applied by the bearing (acting on the rotor) changes, but also when force components and distributions change. Each axis of the MBs has two poles that apply forces in opposite directions. If both forces increase or decrease simultaneously, the strains will change, but the net force acting on the rotor remains constant. Each pole contains 2 primary poles on the axis and 2 auxiliary poles (Figure 40). A change in position could cause a change in the distribution of the forces applied by the primary and auxiliary poles, which again would cause a change in the strain without necessarily causing a change in the net force. Finally, a change in the position of the rotor could change the force distribution within a particular pole. Again, this could cause a change in the strain without causing a change in the net force acting on the rotor. The response associate with the first possibility, strain increasing simultaneously in opposing poles, has not been observed. Position

related strain responses that could be associated with the other two possibilities have been observed, and their effect on test results is substantial. For the IFCM, the position-strain response is larger than the inertial, or applied net force, response for frequencies below 30 Hz.

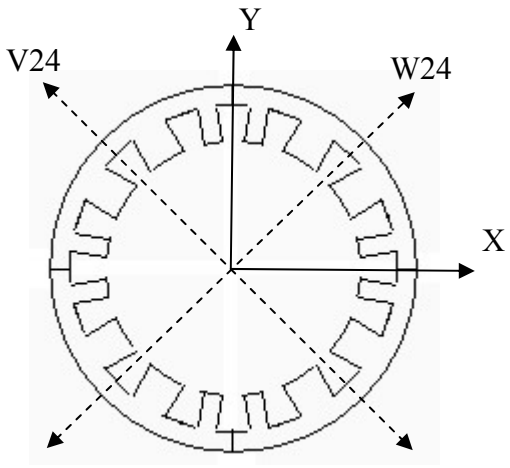

Fig. 40 MB Poles and Axes

Fortunately, the position-dependent strain response is linear, in phase with the inertial force, and significantly smaller than the strain due to inertial force at the higher frequencies. The plots below display the position strain for various injection amplitudes. The frequency of injection is 3 Hz, and the inertial strain at this frequency is roughly 1 % of the position strain. Figures 41 and 42 display the FOSG voltages for S1 and S2 for motions along the V24 and W24 axes.

The position strain is dealt with in one of two ways. One method will be presented later in this section. The first method is to produce the calibration waveform at 3 Hz and subtract the FOSG voltage amplitudes from the amplitudes at higher frequencies. This method is valid if the position-dependent strain is frequency independent and its phase is not altered by the frequency. These assumptions are supported by a linear regression which will be explained later in this section.

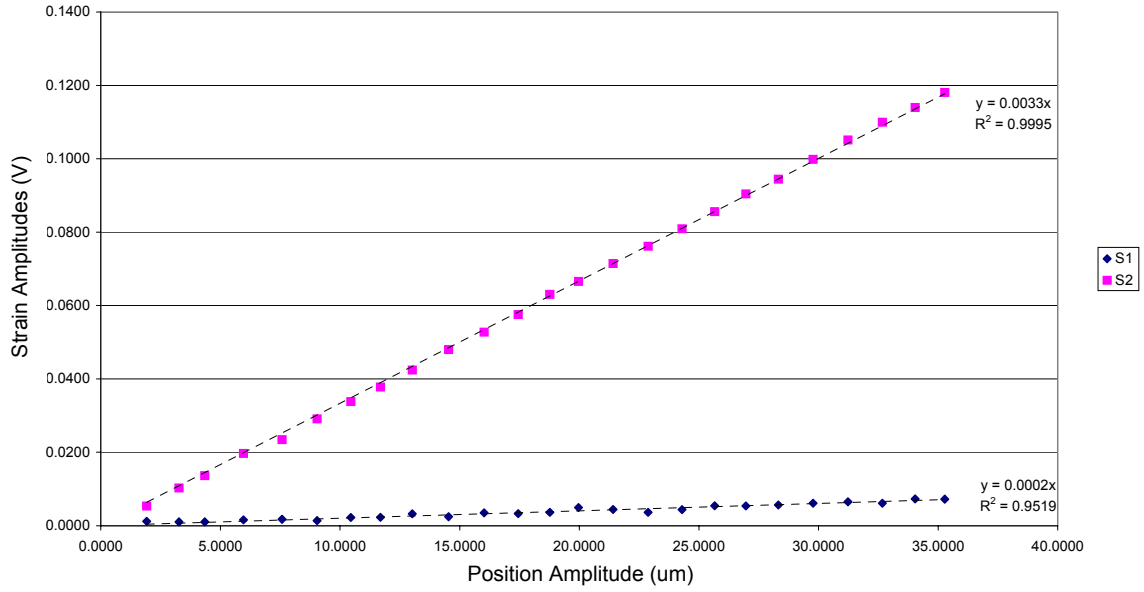

Fig. 41 V24 Axis Position-Dependent Strain

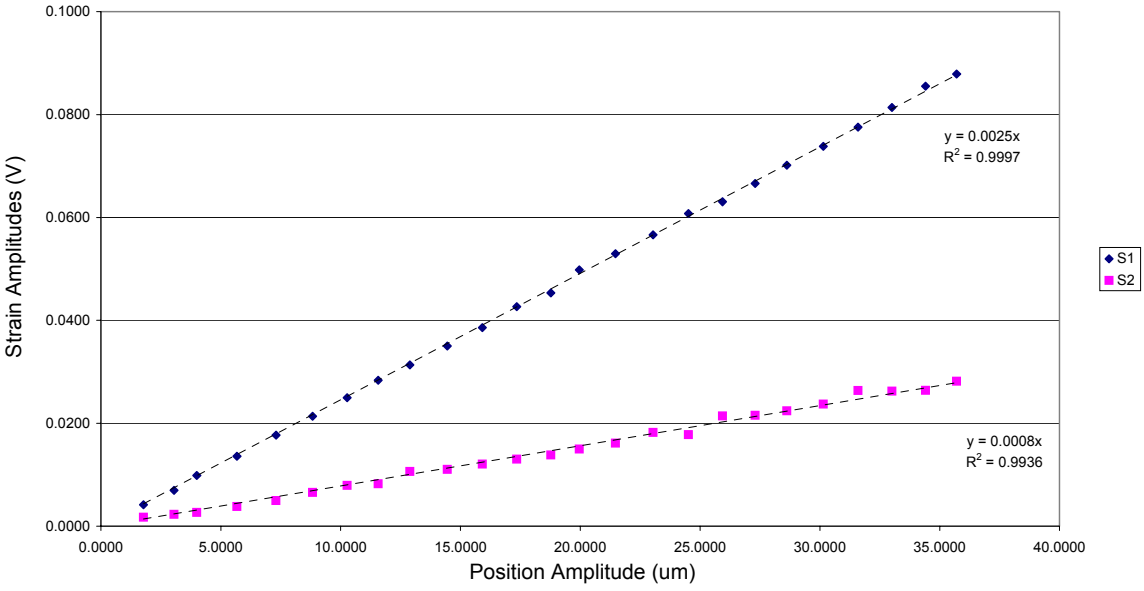

Fig. 42 W24 Axis Position-Dependent Strain

Once the position strain has been removed, a correction is applied to account for the flexibility of the rotor. The inertial force of the rotor is initially calculated assuming the rotor is rigid, and that the motion at both bearings is of the same amplitude and in phase. The assumed mode rotor model was initially used to accommodated rotor flexibility and different absolute position amplitudes at the bearings. The XLTRC^2 model replaced the assumed mode model because it would include absolute position phase differences. The models are used to determine ratios of the flexible rotor model force to the rigid rotor model force. The ratios are then used to correct the strain measurements before the calibration coefficients are determined.

Table 7 displays correction factors for the different models in the vertical and horizontal directions. The assumed mode model agrees well with the more advanced XLTRC^2 model for frequencies below 60 Hz.

Table 7 Comparison of Assumed Mode and FE Models

Flexible Rotor Correction Ratios						
Freq. (Hz)	XLTRC		Assumed Modes		Deviations (%)	
	Horizontal	Vertical	Horizontal	Vertical	Horizontal	Vertical
10	1.006	1.021	1.0078	1.0235	0.2%	0.2%
15	1.008	1.017	1.0100	1.0184	0.2%	0.2%
20	1.015	1.022	1.0159	1.0229	0.1%	0.1%
25	1.022	1.031	1.0223	1.0311	0.1%	0.0%
30	1.043	1.044	1.0449	1.0440	0.2%	0.0%
35	1.063	1.063	1.0619	1.0614	-0.1%	-0.1%
40	1.080	1.085	1.0772	1.0825	-0.2%	-0.3%
45	1.101	1.113	1.0971	1.1085	-0.4%	-0.4%
50	1.125	1.148	1.1200	1.1404	-0.4%	-0.6%
55	1.160	1.191	1.1603	1.1801	0.0%	-0.9%
60	1.296	1.245	1.2931	1.2288	-0.2%	-1.3%
65	1.389	1.316	1.3656	1.2924	-1.7%	-1.8%

The table shows that the assumed mode model underestimates forces at higher frequencies. This outcome is expected because the assumed mode model does not account for rotations of the mass. Neglecting the rotation of the disks probably accounts

for this discrepancy. The forces are slightly overestimated by the assumed mode model at low frequency.

With the corrected strain measurements, the calibration can now be determined. Considering the amplitude of Eq. 17 and converting from radians to Hz produces the following relation.

$$\|F\| = \frac{ml_{cg}}{l} X_0 (2\pi f)^2 \tag{17}$$

The FOSG voltage amplitude is proportional to the applied force. By plotting the FOSG voltage amplitude V divided by the position amplitude for different frequencies against frequency squared, the slope s can be determined. Figure 43 displays a sample plot.

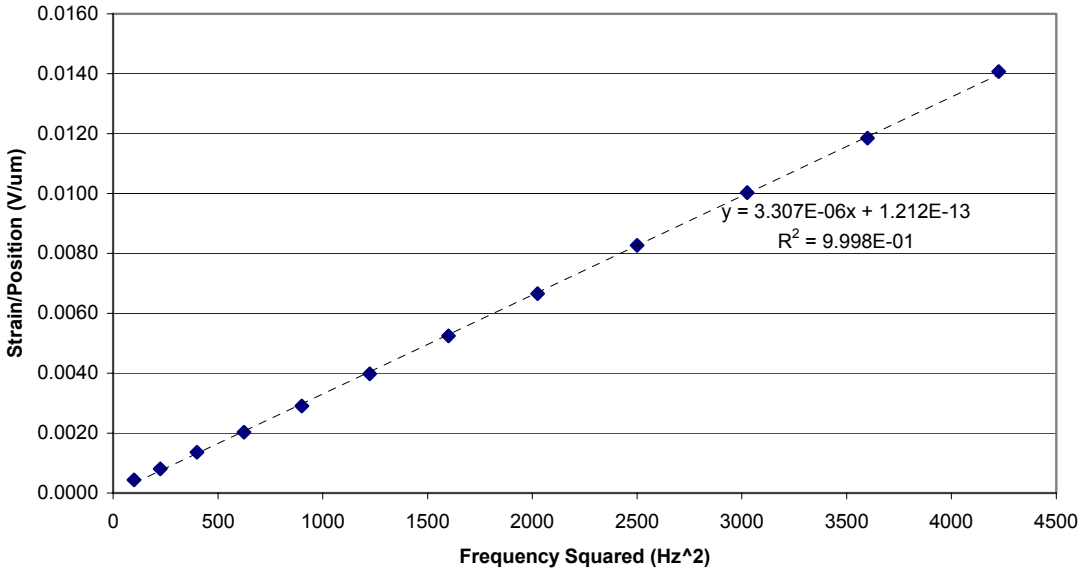

Fig. 43 Sample Inertial FOSG Calibration Plot

Solving Eq. 17 for FOSG voltage divided by position amplitude and frequency squared applying Eq. 15 yields the following equations.

$$F = kV = 4\pi^2 \frac{l_{cg}}{l} X_0 m f^2 \tag{18}$$

$$\frac{V}{X_0 f^2} = \frac{1}{k} 4\pi^2 \frac{l_{cg}}{l} m = s \tag{19}$$

The slope and the system parameters can now determine the calibration coefficient *k*.

$$k = \frac{1}{s} 4\pi^2 \frac{l_{cg}}{l} m \tag{20}$$

The removal of the position-dependent strain can also be accomplished in a second way. The linear regression of the FOSG voltage vs. frequency squared graph also produces a y-axis intercept value. By subtracting the proper voltage (corresponding to the position strain) from the data prior to the flexible rotor correction, the intercept can be controlled. Using the *Goal Seek* feature in Excel, the intercept can be driven to zero. This method is valid if the position strain is frequency independent and its phase is not altered by the frequency. These are the same assumptions that are made for the first method of removing the position strain. The excellent R^2 values in the regressions supports these assumptions.

The calibration matrix **C**, relating strain voltage to force (Eq. 21), can be computed in the following way.

$$\mathbf{F} = \mathbf{C}\ \mathbf{V} \tag{21}$$

The force amplitudes from a horizontal and a vertical shake are represented in the matrix **F**. The FOSG voltage amplitudes from each shake are represented in the columns of the matrix **V**. Subscripts S1 and S2 indicate the FOSG, and the subscripts x and y correspond to horizontal and vertical shakes respectively. The signs are a result of the orientations of the FOSG and shake axes.

$$\mathbf{C}^{-1}\begin{bmatrix} F_x & 0 \\ 0 & F_y \end{bmatrix} = \begin{bmatrix} -V_{S1x} & -V_{S1y} \\ V_{S2x} & -V_{S2y} \end{bmatrix} \tag{22}$$

Post-multiplying the equation by $\mathbf{F}^{-1}$ yields the elements of the $\mathbf{C}^{-1}$ matrix. These terms are simply the reciprocals of the calibration coefficients *k*. The subscripts of the calibration coefficients are the FOSG number and the shake direction respectively.

$$\mathbf{C}^{-1} = \begin{bmatrix} -V_{S1x}/F_x & -V_{S1y}/F_y \\ V_{S2x}/F_x & -V_{S2y}/F_y \end{bmatrix} = \begin{bmatrix} -1/k_{S1x} & -1/k_{S1y} \\ 1/k_{S2x} & -1/k_{S2y} \end{bmatrix} \tag{23}$$

The matrix $\mathbf{C}^{-1}$ can now be inverted to produce the calibration matrix.

$$\mathbf{F} = \begin{bmatrix} -1/k_{S1x} & -1/k_{S1y} \\ 1/k_{S2x} & -1/k_{S2y} \end{bmatrix}^{-1} \mathbf{V} \tag{24}$$

The same procedure is followed for FOSGs 3 and 4 with the only modifications being sign changes. This calibration matrix can now be used to compute forces during a test. Below are sample calibration matrices.

$$\begin{bmatrix} F_x \\ F_y \end{bmatrix}_{12} = \begin{bmatrix} -773.5 & 581.8 \\ -818.7 & -590.6 \end{bmatrix}\begin{bmatrix} V_{S1} \\ V_{S2} \end{bmatrix} \qquad \begin{bmatrix} F_x \\ F_y \end{bmatrix}_{34} = \begin{bmatrix} 687.6 & -716.0 \\ 734.2 & 749.0 \end{bmatrix}\begin{bmatrix} V_{S3} \\ V_{S4} \end{bmatrix} \tag{25}$$

The calibrations for the top and bottom FOSGs are considered separately. During testing, the forces determined by the top and bottom FOSGs are typically averaged to reduce the uncertainty of the measurements. The calibrated FOSGs can now be used to measure forces. First, uncertainties are addressed in the next section.

IFCM: Uncertainty and Discrepancies

The calibrations are not as repeatable as the uncertainties from the FOSG and position measurements suggest. FOSG uncertainties are typically .25% of the maximum calibration FOSG voltage, and position uncertainties are typically .2% or less. However, the calibration changes as time passes; if a calibration is repeated 30 minutes later, it will be nearer the initial calibration than after several hours. The cause of this result is unknown. To determine the uncertainty in the measurements, repeated tests were performed and standard deviations were considered. The rotor was excited vertically at both ends with frequencies from 10 to 90 Hz in 10 Hz increments. Ten tests were performed at each frequency. The standard deviations from the sets of 10 tests were converted from V to N using an approximate force calculated from a flexible rotor model. The tests were repeated 30 minutes to 1 hour later to determine how the calibration would change. This establishes two uncertainties that are considered: uncertainty for a calibration, and uncertainty between calibrations after time/temperature change.

These tests were also performed with and without the use of temperature compensation in the FOSG SCU. Temperature compensation uses non-bonded FOSGs to correct the temperature drift in the FOSG voltages. Tests with and without compensation determine the effectiveness of the temperature compensation and the feasibility of temperature drift causing the calibration uncertainty. Table 8 contains results from the tests without temperature compensation. The uncertainties from a given test for S1 and S2 are typically 2 to 3 N and 1 to 2 N respectively. The *Test Deviation* is the difference in the results of the two tests. This means that if a calibration were performed immediately prior to Test 1, after 30 minutes to 1 hour passes, the error in the calibration could be

characterized by the deviation between the two tests. In practice, reducing the time required for testing after calibrating would improve the uncertainty. The deviation in the test could be determined by calibrating before and after the test. The last two columns are the deviation as a percent of bearing load capacity and a percent of the test (inertial) load. Table 9 displays the results for the tests with temperature compensation.

Table 8 Test Deviations without Temperature Compensation

	Frequecy (Hz)	Test 1 Uncert. (N)	Test 2 Uncert. (N)	Test Dev. (N)	Dev. % of LC	Dev. % of Test Load
S1	10	2.359	0.925	1.878	0.05%	60%
	20	0.892	0.862	3.575	0.09%	28%
	40	2.020	1.793	4.236	0.11%	8%
	50	1.625	2.171	4.232	0.11%	5%
	60	2.431	3.265	5.939	0.15%	4%
	70	2.670	3.314	11.349	0.29%	5%
	80	4.052	3.002	12.780	0.32%	4%
	90	3.711	3.870	8.002	0.20%	1%
S2	Frequecy (Hz)	Test 1 Uncert. (N)	Test 2 Uncert. (N)	Test Dev. (N)	Dev. % of LC	Dev. % of Test Load
	10	0.763	0.782	0.326	0.01%	10%
	20	0.660	0.511	0.506	0.01%	4%
	40	1.967	0.988	1.611	0.04%	3%
	50	1.448	0.575	3.472	0.09%	4%
	60	1.836	0.760	4.870	0.12%	4%
	70	1.325	0.840	5.438	0.14%	3%
	80	1.318	1.173	9.460	0.24%	3%
	90	1.539	1.061	5.647	0.14%	1%

The results from the temperature compensated tests do not exhibit any improvements over the uncompensated tests. This indicates that the temperature compensation is either not operating correctly or is not causing the calibration change. Further investigation into the temperature compensation algorithm revealed that the compensation only affects measurement that are considered at or below the temperature drift frequencies. In fact, the compensation does not adjust the FOSG sensitivity and therefore has no affect on

Table 9 Test Deviations with Temperature Compensation

	Frequecy (Hz)	Test 1 Uncert. (N)	Test 2 Uncert. (N)	Test Dev. (N)	Dev. % of LC	Dev. % of Test Load
S1	10	2.359	0.953	1.935	0.05%	61%
	20	0.892	0.747	3.834	0.10%	30%
	40	2.020	2.046	6.060	0.15%	11%
	50	1.625	1.852	5.704	0.14%	6%
	60	2.431	2.607	8.490	0.21%	6%
	70	2.670	2.430	12.843	0.33%	6%
	80	4.052	3.662	17.885	0.45%	5%
	90	3.711	3.604	2.795	0.07%	0%
S2	Frequecy (Hz)	Test 1 Uncert. (N)	Test 2 Uncert. (N)	Test Dev. (N)	Dev. % of LC	Dev. % of Test Load
	10	0.763	0.942	0.083	0.00%	3%
	20	0.660	0.597	0.599	0.02%	5%
	40	1.967	0.965	4.126	0.10%	8%
	50	1.448	0.810	5.556	0.14%	6%
	60	1.836	0.721	4.496	0.11%	3%
	70	1.325	0.881	4.789	0.12%	2%
	80	1.318	1.257	9.124	0.23%	3%
	90	1.539	0.810	3.624	0.09%	1%

dynamic measurements. However, other applications of FOSGs have determined that the sensor sensitivities change only slightly for temperature changes as large as 360 °F (200 °C). The temperatures for the FOSGs in the MBs have a range of at most 10 to 15 °F (18 to 27 °C). As a result, it is unlikely that temperature drift is the cause of the calibration change. The FOSGs are typically used to measure larger strain values than are observed in the MBs, and a test program to examine FOSG measurement repeatability for small strains is presently being considered.

The other unresolved issue is the discrepancy between the vertical and the horizontal calibrations. The calibration coefficients and the slopes for the linear regressions are different depending on the direction of the excitation. By first determining whether the errors are systematic or random, the possible causes of the discrepancy can be reduced.

Table 10 shows the regression slopes from 6 different pairs of vertical and horizontal tests and the percent deviation between the slopes of each pair.

Table 10 Regression Slopes and Deviations

Combined Test Results: Regression Slopes					
		FOSG 1	FOSG 2	FOSG 3	FOSG 4
Set 1	H	2.54E-06	3.35E-06	2.93E-06	2.76E-06
	V	2.36E-06	3.34E-06	2.73E-06	2.63E-06
Set 2	H	2.57E-06	3.40E-06	2.93E-06	2.81E-06
	V	2.43E-06	3.37E-06	2.74E-06	2.66E-06
Set 3	H	2.58E-06	3.41E-06	2.91E-06	2.81E-06
	V	2.43E-06	3.31E-06	2.72E-06	2.67E-06
Set 4	H	2.57E-06	3.38E-06	2.89E-06	2.81E-06
	V	2.44E-06	3.35E-06	2.75E-06	2.69E-06
Set 5	H	2.54E-06	3.38E-06	2.85E-06	2.71E-06
	V	2.37E-06	3.29E-06	2.65E-06	2.62E-06
Set 6	H	2.58E-06	3.43E-06	2.90E-06	2.79E-06
	V	2.44E-06	3.38E-06	2.72E-06	2.67E-06
Vertical and Horizontal Deviations					
		FOSG 1	FOSG 2	FOSG 3	FOSG 4
Set 1		-7%	0%	-7%	-5%
Set 2		-6%	-1%	-7%	-5%
Set 3		-6%	-3%	-7%	-5%
Set 4		-6%	-1%	-5%	-4%
Set 5		-7%	-3%	-8%	-4%
Set 6		-6%	-2%	-7%	-4%

The deviations are reasonably systematic. The negative percentages indicate that the horizontal slopes are in all cases larger than the vertical slopes. One possibility is that this is not an error, but that the FOSGs actually respond differently to horizontal and vertical forces. If this is true, one would expect an angle of maximum sensitivity other than 45°. Tests were performed to explore this possibility.

The rotor was excited at various angles from each of the FOSG axes. Initially, the tests were performed at 15 Hz. However, the inertial forces at this frequency were too low to produce conclusive results. The tests were repeated at 40 Hz. Figures 44 and 45 display FOSG voltage amplitudes as a function of the excitation angle. The angle is measured

from the V24 axis and toward the vertical axis. An angle of 0° denotes alignment with the V24 axis and 90° denotes alignment with the W24 axis.

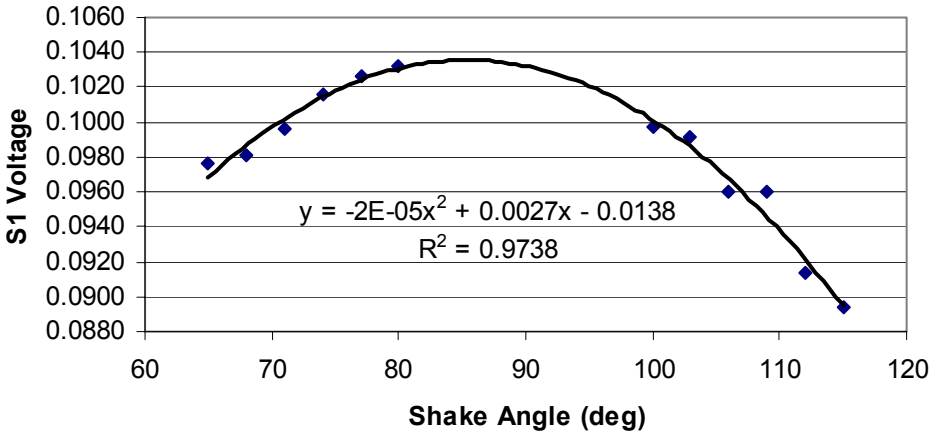

Fig. 44 Force Angle Test Results for S1

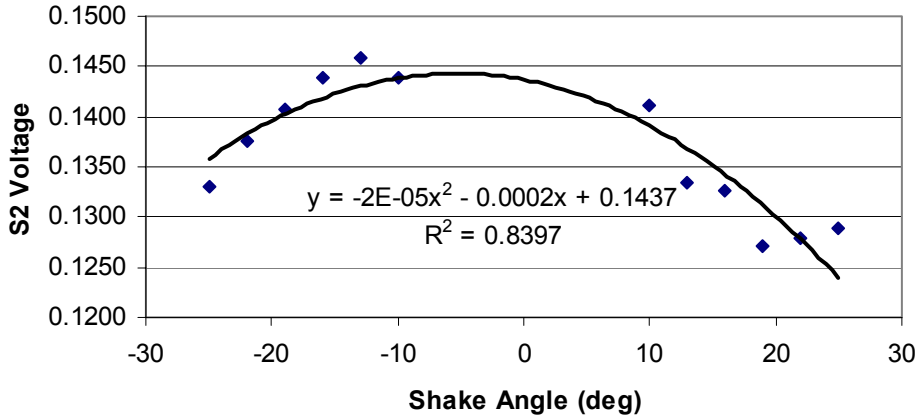

Fig. 45 Force Angle Test Results for S2

These shake angles are based on the proximity probe position measurements. By using the accelerometer measurements, the absolute positions are determined and Figures 46

and 47 are produced. Strain voltage is divided by the shake amplitude because the absolute position amplitudes differ for the various angles.

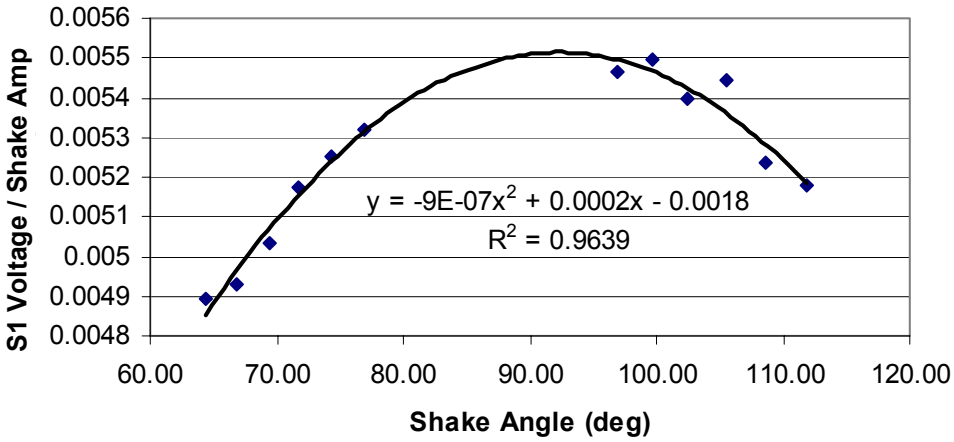

Fig. 46 Force Angle Test Results for S1 with Accelerometer Measurements

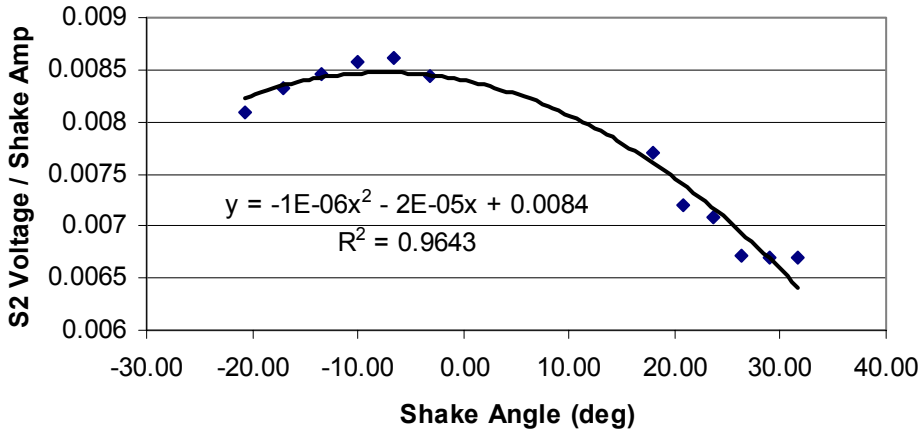

Fig. 47 Force Angle Test Results for S2 with Accelerometer Measurements

Referring to the graphs based on absolute position, the angle of maximum sensitivity for S1 is above 90° which indicates more sensitivity in the horizontal direction. For S2 the angle is less than 0 also suggesting more sensitivity in the horizontal direction. These

results correlate to some degree with the findings from the previous repeated tests. Angles of maximum sensitivity can also be determined for the repeated tests. Table 11 displays deviation averages of Table10 and the angle of maximum sensitivity in degrees measured from the FOSG axis toward the horizontal.

Table 11 Maximum Sensitivity Angles

	Avg. Dev.	Angle (deg)
FOSG 1	-6%	1.9
FOSG 2	-1%	0.4
FOSG 3	-7%	2.0
FOSG 4	-5%	1.4

The results from the angle excitation tests suggest that the angles of maximum sensitivity are around 5° to 10° from the FOSG axes. While the two tests produce similar conclusions, the accuracy of the tests is still unknown. In addition, the suggestion that all the FOSG are more sensitive in the horizontal direction than the vertical direction seems suspicious. The possibility of random error has been eliminated as a cause of this discrepancy, but the possibility for systematic error still exists. An error in the calibration model could produce a systematic error. The horizontal calibration relies more heavily on the modeling because the bearing motion, in the horizontal calibration, results in different amplitudes and phases for the rotor ends. If there is an angle of maximum sensitivity, it is not clear what this would mean. The geometry of the magnetic bearing prevents FOSG misalignment for creating the same effects that might occur with a solid object. This discrepancy could also indicate a misalignment in the proximity probe coordinate systems.

IFCM Conclusions

An Inertial FOSG Calibration with acceptable accuracy has been demonstrated and rotordynamic testing will now be considered. The data reduction process resolves many issues that confronted the first Inertial FOSG Calibration attempts. The Labview

programs can be used to accurately calibrate and quickly perform tests, reducing the effects of the calibration drift. The calibration drift can also be addressed by calibrating before and after a test. The final unresolved issue of vertical and horizontal calibration is clearly systematic. The discrepancy is caused either by an actual physical phenomena affecting the FOSG measurements, by a model error, or by a dynamic response that is undetected and unaccounted for. The overall uncertainties in the FOSG forces range from 1 to 2 lbf (4 to 9 N) depending on the FOSG. This translates to less than .3% of load capacity and is acceptable. The calibrated FOSG forces are now utilized in rotordynamic testing.

IV. DYNAMIC FLEXIBILITY TRANSFER FUNCTION IDENTIFICATION

Explanation and Derivation of DFTFs

With a successful Inertial FOSG Calibration, a variety of rotordynamic phenomena can be tested. It is now feasible for test programs to utilize MBs as calibrated exciters and perform parameter identification of rotor properties, seal coefficients, and even impeller coefficients. However, a rotordynamic test must first be performed to validate the MB test methodology. By identifying dynamic flexibility transfer functions (DFTFs), results can such as rotor speed dependent natural frequencies can be compared with predictions from XLTRC^2 to validate the test method.

Mathematical Derivations of DFTFs

Stiffness K describes force F as a function of position X, and flexibility G, which describes position as a function of force, is the inverse of stiffness.

$$\left.\begin{aligned} F &= K\,X \\ X &= G\,F \end{aligned}\right\} \Rightarrow G = K^{-1} \tag{26}$$

For a spring, the relationship between force and position is constant (frequency independent). So the flexibility transfer function is simply the inverse of the spring stiffness coefficient. For a more complex system, the position response to the force can vary significantly in amplitude and phase as a function of excitation frequency. A single degree of freedom harmonic oscillator can exhibit responses ranging from resonance with large amplitudes as rapid phase shifts to isolation where the response can be undetectable. As in the case of MB test rig, variation in other states of the system can affect the transfer functions. Rotor speed causes gyroscopic coupling of the vertical and

horizontal responses. The rotor speed dependent transfer functions are referred to as dynamic flexibility transfer functions. A two degree of freedom system DFTF can be determined as follows. First terms of the flexibility matrix are assigned. The first subscript indicates the force direction, and the second indicates the position response direction. For example, G_{xy} is the transfer function from the force in the x-direction to the position in the y-direction.

$$\begin{bmatrix} x \\ y \end{bmatrix} = \begin{bmatrix} G_{xx} & G_{yx} \\ G_{xy} & G_{yy} \end{bmatrix} \begin{bmatrix} F_x \\ F_y \end{bmatrix} \tag{27}$$

Two tests can be performed to determine the components of the flexibility matrix. Typically either the force or the position is constrained to be the x-direction for one shake and the y-direction for the other. To preserve generality, none of the force of position components will be set to zero. Subscripts x and *y* refer to the shake directions of the tests. In the case of the force vector components, the first subscript indicates the force direction, and the second indicates the shake direction of the test.

$$\mathbf{X}_x = \begin{bmatrix} x_x \\ y_x \end{bmatrix} \qquad \mathbf{F}_x = \begin{bmatrix} F_{xx} \\ F_{yx} \end{bmatrix} \tag{28}$$

$$\mathbf{X}_y = \begin{bmatrix} x_y \\ y_y \end{bmatrix} \qquad \mathbf{F}_y = \begin{bmatrix} F_{xy} \\ F_{yy} \end{bmatrix} \tag{29}$$

Force and position vectors from the two tests can combined as follows to produce a matrix equation.

$$\begin{bmatrix} \mathbf{X}_x & \mathbf{X}_y \end{bmatrix} = \mathbf{G} \begin{bmatrix} \mathbf{F}_x & \mathbf{F}_y \end{bmatrix} \quad \Leftrightarrow \quad \begin{bmatrix} x_x & x_y \\ y_x & y_y \end{bmatrix} = \begin{bmatrix} G_{xx} & G_{yx} \\ G_{xy} & G_{yy} \end{bmatrix} \begin{bmatrix} F_{xx} & F_{xy} \\ F_{yx} & F_{yy} \end{bmatrix} \tag{30}$$

By post-multiplying the position matrix with the inverse of the force matrix, the flexibility matrix is determined.

$$\begin{bmatrix} G_{xx} & G_{yx} \\ G_{xy} & G_{yy} \end{bmatrix} = \begin{bmatrix} x_x & x_y \\ y_x & y_y \end{bmatrix} \begin{bmatrix} F_{xx} & F_{xy} \\ F_{yx} & F_{yy} \end{bmatrix}^{-1} \tag{31}$$

The flexibility transfer function is determined by repeating the above process for a range of forcing frequencies. For a DFTF, flexibility transfer functions are determined over a range of rotor speeds. The result is a characterization of the system's position response to input forces as a function of forcing frequency and rotor speed.

System Model

A better understanding of the MB test rig will assist in the understanding of later results. The physical model for the system is displayed in Figure 48. A flexible rotor with a significant polar moment of inertia is constrained at one end by springs and dampers in both the vertical and horizontal directions. The other end of the rotor is affected of by the input forces F_x and F_y. The MB without FOSGs is regarded as springs and dampers because the position will not be controlled as an input parameter. In reality, the force applied by the MB without FOSGs is better described by transfer functions, but the present model suffices to illustrate its affects. The MB with FOSGs is represented by the force inputs. This is because the FOSGs provide measurements for the total net force of the MB. The system is expected to exhibit characteristics of high flexibility at low frequencies, decreasing flexibility with increasing frequency, and local increases in flexibility around rotor and MB natural frequencies.

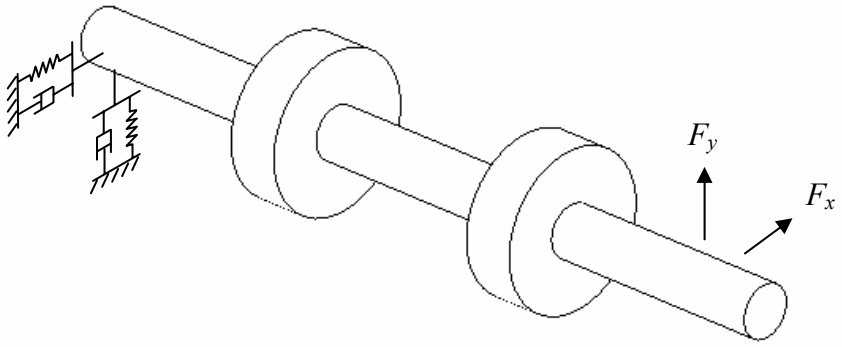

Fig. 48 MB Test Rig System Model for DFTF Testing

Theoretical Example of Gyroscopic Coupling in DFTFs

Simulating the effects of gyroscopic coupling on a less complex system will illustrate the characteristic of interest in experimental results of the MB test rig. A disc with large polar inertia is overhung on a small flexible shaft (Figure 49). This system is known as the Stodola-Green model and is commonly used to illustrate gyroscopic effects in rotordynamics.

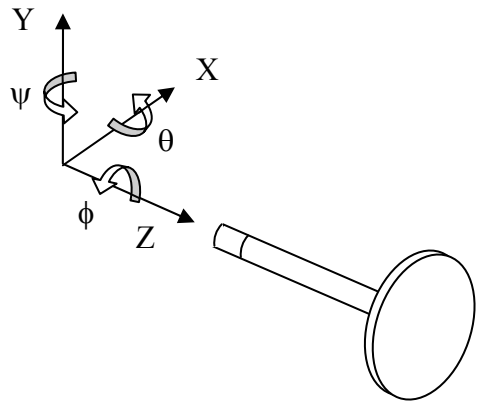

Fig. 49 Stodola-Green Rotor Model for Theoretical Example

The equations of motion are derived by first determining the angular velocity vector ω and the angular acceleration vector α. The angles θ, ψ, and ϕ describe rotations about the X, Y and Z axes respectively.

$$\boldsymbol{\omega} = \begin{bmatrix} \dot{\theta} \\ \dot{\psi} \\ \dot{\phi} \end{bmatrix} \qquad \boldsymbol{\alpha} = \begin{bmatrix} \ddot{\theta} + \dot{\psi}\dot{\varphi} \\ \ddot{\psi} - \dot{\theta}\dot{\varphi} \\ \ddot{\phi} - \dot{\psi}\dot{\theta} \end{bmatrix} \tag{32}$$

Torque $\boldsymbol{\Gamma}$ due to accelerations and gyroscopic coupling can be computed using the Euler equation (Eq. 33). The inertia matrix $\mathbf{I}$ contains moment of inertia I_2 for the X and Y axes, and I_1 for the Z axis. $\hat{\boldsymbol{\omega}}$ is the angular velocity tensor.

$$\boldsymbol{\Gamma} = \mathbf{I}\,\boldsymbol{\alpha} + \hat{\boldsymbol{\omega}}\,\mathbf{I}\,\boldsymbol{\omega} \tag{33}$$

The components of resulting vector are displayed below. Subscripts X, Y and Z indicate the axis about which the torque acts. The change in the rotor speed $\dot{\phi}$ due to angular velocities $\dot{\psi}$ and $\dot{\theta}$ can be neglected for large $\dot{\phi}$ and sinusoidal $\dot{\psi}$ and $\dot{\theta}$ over small angles. The equation for the rotor acceleration can therefore be omitted from the calculation when $\dot{\phi}$ is considered constant.

$$\begin{bmatrix} \Gamma_X \\ \Gamma_Y \\ \Gamma_Z \end{bmatrix} = \begin{bmatrix} I_2\ddot{\theta} + I_1\dot{\psi}\dot{\phi} \\ I_2\ddot{\psi} - I_1\dot{\theta}\dot{\phi} \\ I_1\left(\ddot{\phi} - \dot{\psi}\dot{\theta}\right) \end{bmatrix} \tag{34}$$

The stiffness matrix due to elastic reaction forces and moments exerted by the shaft is based on linear elastic theory [12]. Elastic modulus E, area moment of inertia I_A, and shaft length L are the parameters that determine the stiffness.

$$\begin{bmatrix} f_X \\ \tau_Y \\ f_Y \\ \tau_X \end{bmatrix} = \frac{-12EI_A}{L^3} \begin{bmatrix} 1 & -L/2 & 0 & 0 \\ -L/2 & L^2/3 & 0 & 0 \\ 0 & 0 & 1 & L/2 \\ 0 & 0 & L/2 & L^2/3 \end{bmatrix} \begin{bmatrix} X \\ \psi \\ Y \\ \theta \end{bmatrix} \tag{35}$$

Considering linear momentum equations and combining Eq. 34 and 35 yields the Eq. 36. Rotor mass m, forces F_x and F_y, and moments M_x and M_y are introduced.

$$\begin{bmatrix} m & 0 & 0 & 0 \\ 0 & I_2 & 0 & 0 \\ 0 & 0 & m & 0 \\ 0 & 0 & 0 & I_2 \end{bmatrix} \begin{bmatrix} \ddot{X} \\ \ddot{\psi} \\ \ddot{Y} \\ \ddot{\theta} \end{bmatrix} + \begin{bmatrix} 0 & 0 & 0 & 0 \\ 0 & 0 & 0 & -I_1\dot{\phi} \\ 0 & 0 & 0 & 0 \\ 0 & I_1\dot{\phi} & 0 & 0 \end{bmatrix} \begin{bmatrix} \dot{X} \\ \dot{\psi} \\ \dot{Y} \\ \dot{\theta} \end{bmatrix} + \frac{12EI}{L^3} \begin{bmatrix} 1 & -L/2 & 0 & 0 \\ -L/2 & L^2/3 & 0 & 0 \\ 0 & 0 & 1 & L/2 \\ 0 & 0 & L/2 & L^2/3 \end{bmatrix} \begin{bmatrix} X \\ \psi \\ Y \\ \theta \end{bmatrix} = \begin{bmatrix} F_X \\ M_Y \\ F_Y \\ M_X \end{bmatrix} \tag{36}$$

External moments are not include in further derivations because the external forces will provide an adequate example. The equations can be non-dimensionalized using the following substitutions:

$$\begin{aligned} t_N &= \beta t & \omega_N &= \frac{\dot{\phi}}{\beta} & \beta &= \sqrt{\frac{12EI}{mL^3}} \\ X_N &= \eta X & Y_N &= \eta Y & \eta &= \frac{12EI}{mL^3}\frac{1}{\|F_X\|} \\ \psi_N &= \gamma\psi & \theta_N &= \gamma\theta & \gamma &= \frac{12EI}{mL^2}\frac{1}{\|F_X\|} \end{aligned} \tag{37}$$

Eq. 38 is the non-dimensional equation of motions. The inertia ratio r_I and the mass ratio r_m are given in Eq. 39.

$$\begin{bmatrix} 1 & 0 & 0 & 0 \\ 0 & 1 & 0 & 0 \\ 0 & 0 & 1 & 0 \\ 0 & 0 & 0 & 1 \end{bmatrix} \begin{bmatrix} \ddot{X}_N \\ \ddot{\psi}_N \\ \ddot{Y}_N \\ \ddot{\theta}_N \end{bmatrix} + \begin{bmatrix} 0 & 0 & 0 & 0 \\ 0 & 0 & 0 & -r_I\omega_N \\ 0 & 0 & 0 & 0 \\ 0 & r_I\omega_N & 0 & 0 \end{bmatrix} \begin{bmatrix} \dot{X}_N \\ \dot{\psi}_N \\ \dot{Y}_N \\ \dot{\theta}_N \end{bmatrix} + \begin{bmatrix} 1 & -\frac{1}{2} & 0 & 0 \\ -\frac{1}{2}r_m & \frac{1}{3}r_m & 0 & 0 \\ 0 & 0 & 1 & \frac{1}{2} \\ 0 & 0 & \frac{1}{2}r_m & \frac{1}{3}r_m \end{bmatrix} \begin{bmatrix} X_N \\ \psi_N \\ Y_N \\ \theta_N \end{bmatrix} = \begin{bmatrix} F_X/\|F_X\| \\ 0 \\ F_Y/\|F_Y\| \\ 0 \end{bmatrix} \tag{38}$$

$$r_I = \frac{I_1}{I_2} \qquad r_m = \frac{mL^2}{I_2} \tag{39}$$

External damping is added to produced finite response responses when transfer functions are determined. The external damping is twice the damping ratio multiplied by the square root of the non-dimensionalized direct stiffness.

$$\begin{bmatrix} 1 & 0 & 0 & 0 \\ 0 & 1 & 0 & 0 \\ 0 & 0 & 1 & 0 \\ 0 & 0 & 0 & 1 \end{bmatrix} \begin{bmatrix} \ddot{X}_N \\ \ddot{\psi}_N \\ \ddot{Y}_N \\ \ddot{\theta}_N \end{bmatrix} + \begin{bmatrix} 2\xi & 0 & 0 & 0 \\ 0 & 2\xi\sqrt{\tfrac{1}{3}r_m} & 0 & -r_I\omega_N \\ 0 & 0 & 2\xi & 0 \\ 0 & r_I\omega_N & 0 & 2\xi\sqrt{\tfrac{1}{3}r_m} \end{bmatrix} \begin{bmatrix} \dot{X}_N \\ \dot{\psi}_N \\ \dot{Y}_N \\ \dot{\theta}_N \end{bmatrix} + \begin{bmatrix} 1 & -\tfrac{1}{2} & 0 & 0 \\ -\tfrac{1}{2}r_m & \tfrac{1}{3}r_m & 0 & 0 \\ 0 & 0 & 1 & \tfrac{1}{2} \\ 0 & 0 & \tfrac{1}{2}r_m & \tfrac{1}{3}r_m \end{bmatrix} \begin{bmatrix} X_N \\ \psi_N \\ Y_N \\ \theta_N \end{bmatrix} = \begin{bmatrix} F_X / \|F_X\| \\ 0 \\ F_Y / \|F_Y\| \\ 0 \end{bmatrix} \quad (40)$$

By the converting the system to state-space representation, it can be analyzed in the frequency domain. The transfer functions are computed using the system matrix A and assigning B and C matrices. The B and C matrices below correspond to an input force $F_X / \|F_X\|$ and outputs X_N and Y_N.

$$\mathbf{B} = \begin{bmatrix} 0 & 0 & 0 & 0 & 1 & 0 & 0 & 0 \end{bmatrix}^T \qquad \mathbf{C} = \begin{bmatrix} 1 & 0 & 0 & 0 & 0 & 0 & 0 & 0 \\ 0 & 1 & 0 & 0 & 0 & 0 & 0 & 0 \end{bmatrix} \quad (41)$$

The damping ratio ξ was selected to be low enough to clearly distinguish natural frequency peaks. The inertia ratio r_I is calculated for a disk, and the inertial properties of the shaft are is neglected. The mass ratio r_m can reduces to a function of the ratio between the shaft length and the disk radius. The mass ratio is calculated for the shaft length equal to the disk radius. The non-dimensional rotor speed ω_N was selected to produce noticeable gyroscopic coupling. Table 12 contains the values of these parameters

Table 12 Parameters for Theoretical Example

Parameter	Value
ξ	.03
r_I	2
r_m	4
ω_N	0, .2

Figure 50 displays the amplitudes and phases of the X_N and Y_N due to input $F_X / \|F_X\|$ for zero rotor speed. This results exhibit no coupling between X_N and Y_N. The two resonances are zero-speed natural frequencies that correspond to two different modes. Figure 51 displays the same results for ω_N equal to .2. Coupling is evident, and four resonances are visible. The resonances correspond to the forward and backward critical speeds associated with the previous zero-speed natural frequencies

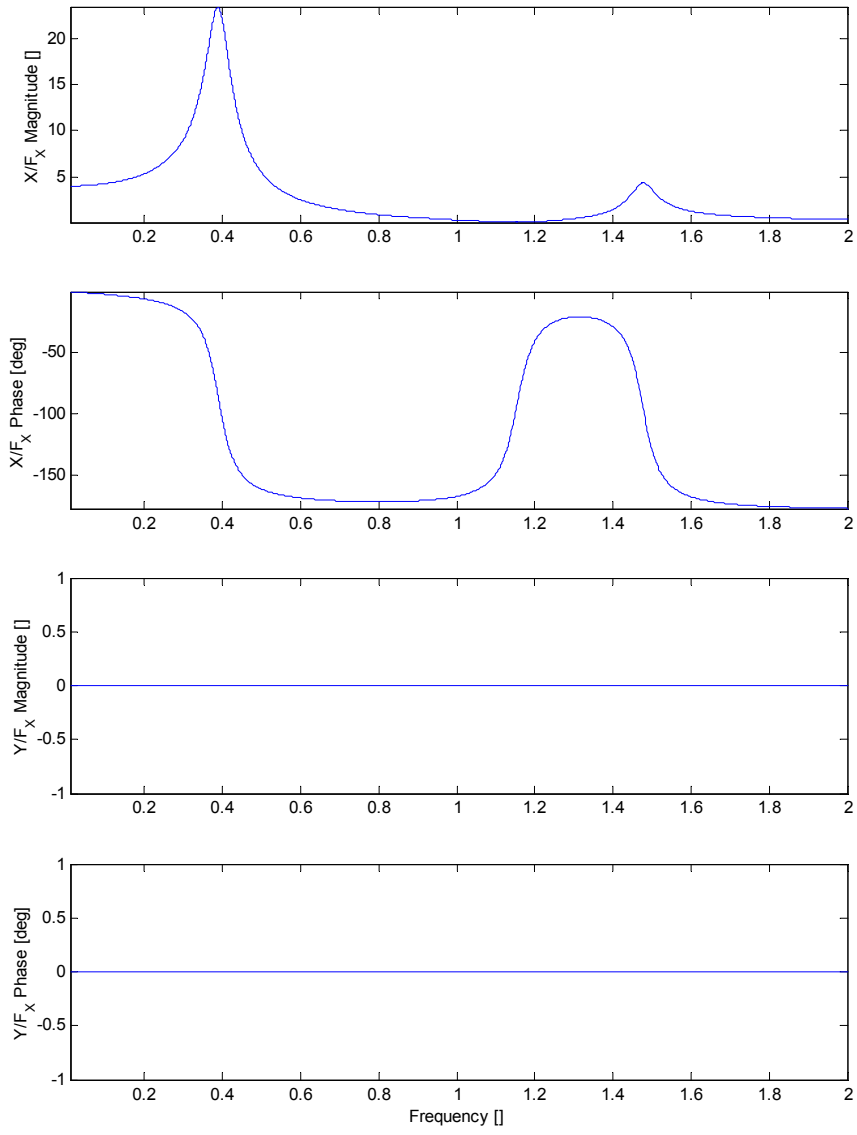

Fig. 50 Frequency Response- Zero Rotor Speed

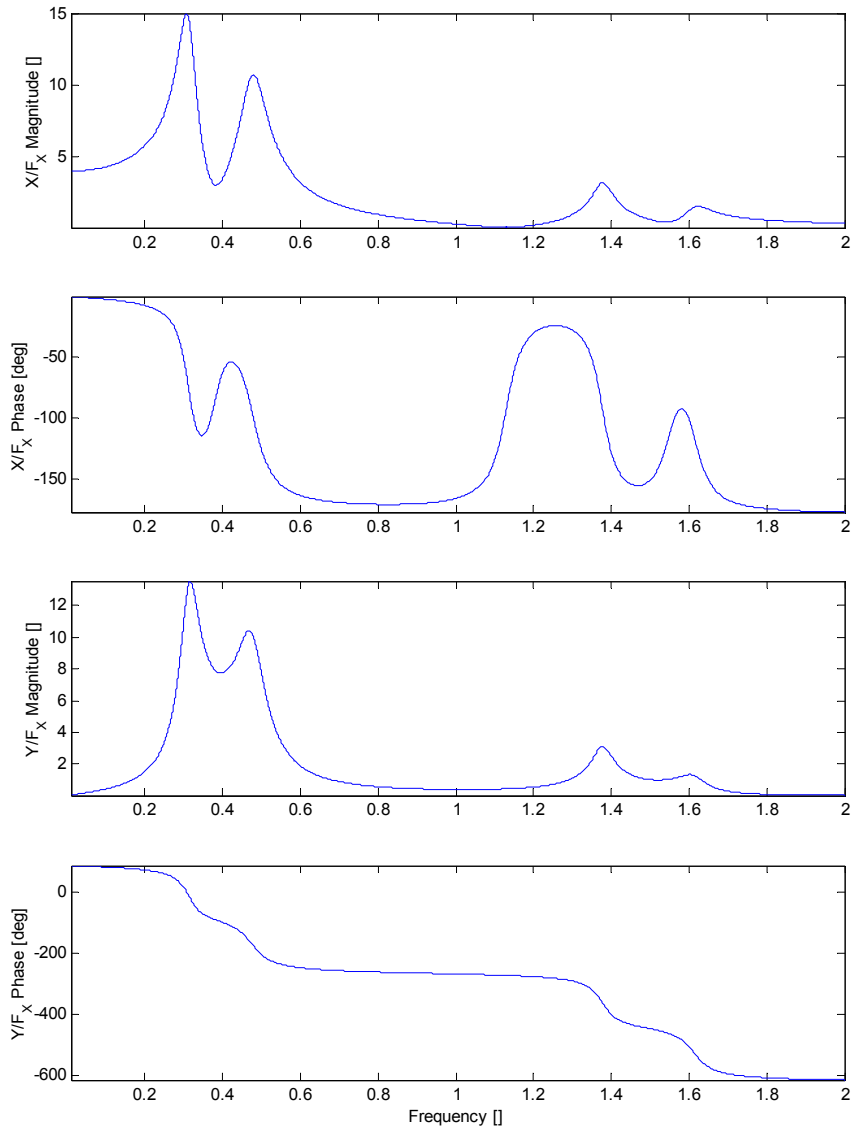

Fig. 51 Frequency Response- Constant Rotor Speed

DFTF Testing and Results

The DFTF testing experimental procedure is very similar to that of the IFCM. Waveforms are injected through the MBResearch Panel. As mention in the previous section, only the MB with FOSGs is controlled with the injection signal. Vertical and horizontal directions are excited at frequencies ranging from 80 to 180 Hz. Frequency

spacing varies to emphasize results near the first bending mode of the rotor. The amplitudes of the shakes are 10 μm. As described in the IFCM section, a Labview VI iterates to obtain desirable injection characteristics. The data from the FOSGs, proximity probes, and accelerometers are acquired and saved for acceptable injections. Data reduction is performed using Excel spreadsheets. The position-dependent strain is removed, and the FOSGs voltages are converted into vertical and horizontal forces using the calibration determined by the IFCM. DFTFs are computed as described in the *Mathematical Derivation of DFTFs* section. DFTFs are computed for rotor speed of 0 to 5000 rpm by 1000 rpm intervals. Uncertainties are determined based on standard deviations of 10 repeated tests at 0 rpm.

Figures 52 through 59 display the amplitudes and phases of the DFTF components. G_{xx} and G_{yy} are the direct terms for the horizontal and vertical directions respectively. G_{xy} and G_{yx} are the cross coupled terms relating horizontal force to vertical response and vertical force to horizontal response respectively. Uncertainties are displayed by the standard deviations plotted on the frequency axes.

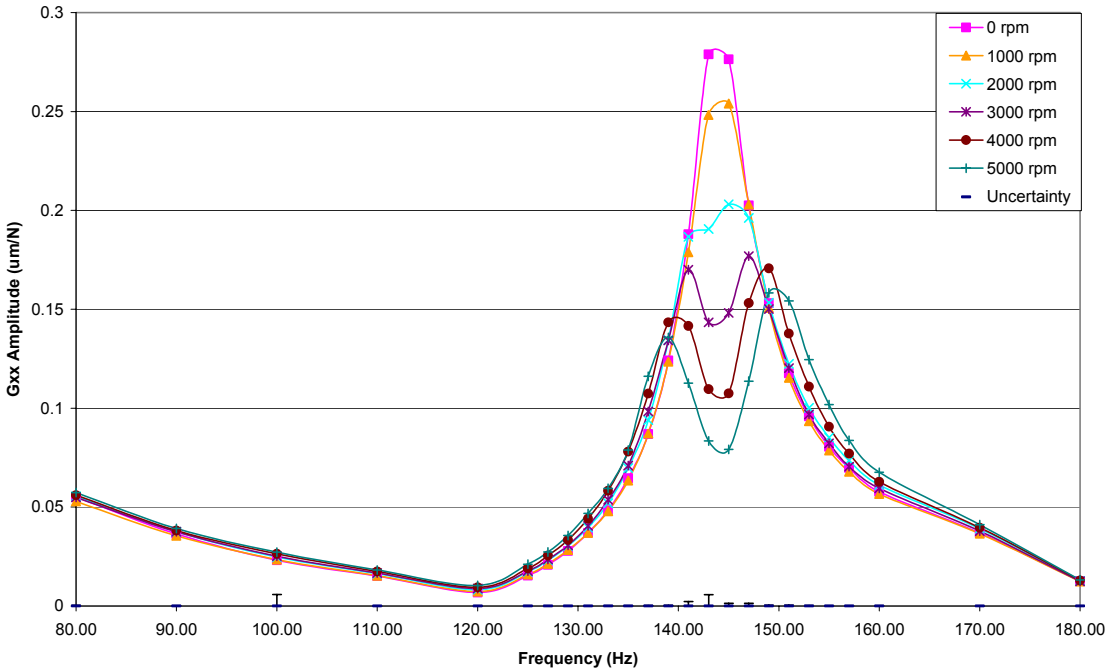

Fig. 52 G_{xx} Amplitude Plot

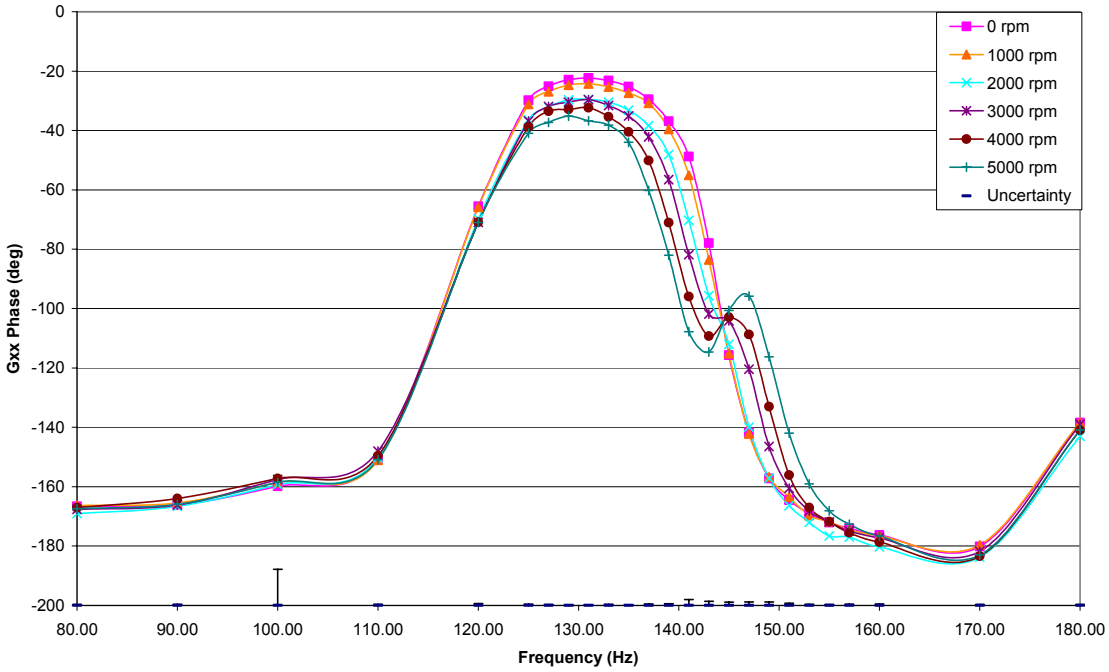

Fig. 53 G_{xx} Phase Plot

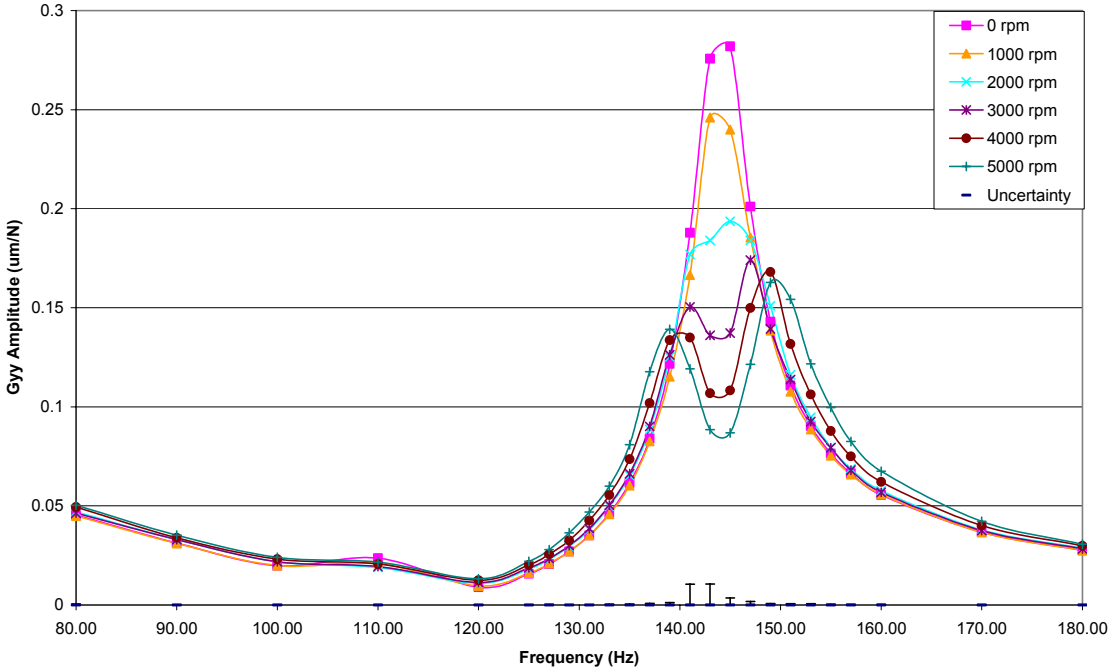

Fig. 54 G_{yy} Amplitude Plot

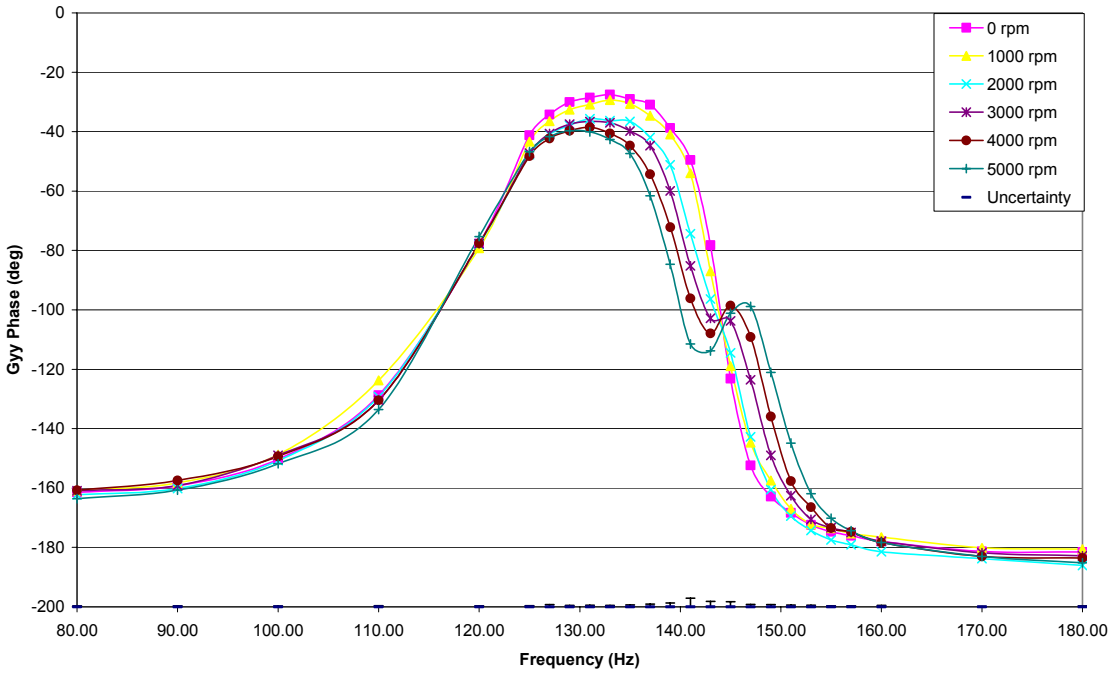

Fig. 55 G_{yy} Phase Plot

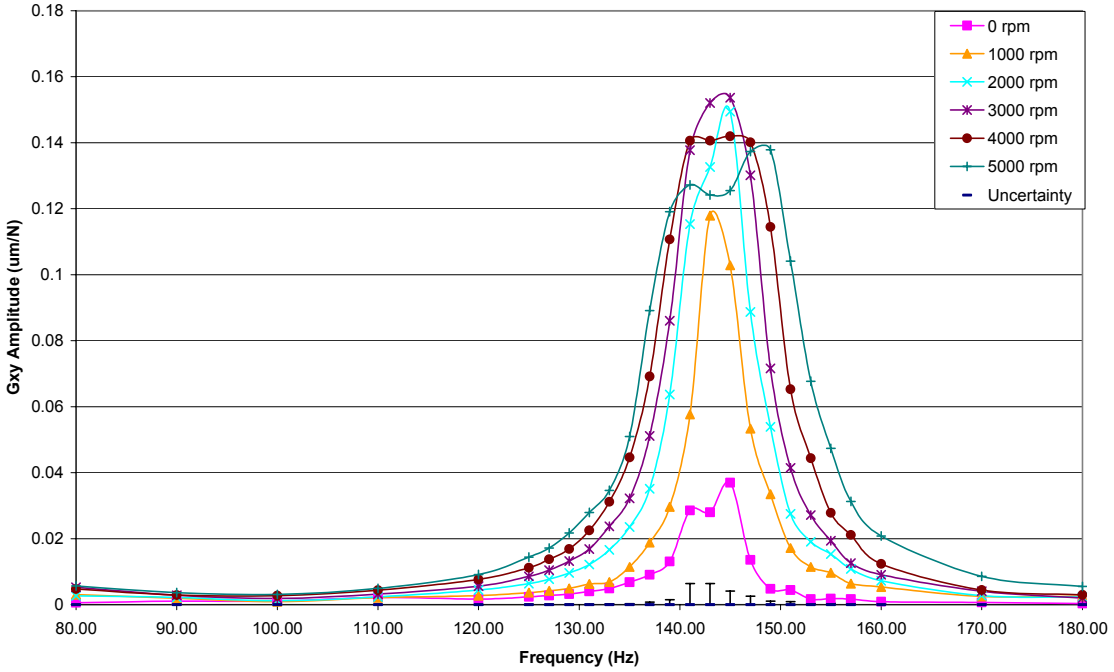

Fig. 56 G_{xy} Amplitude Plot

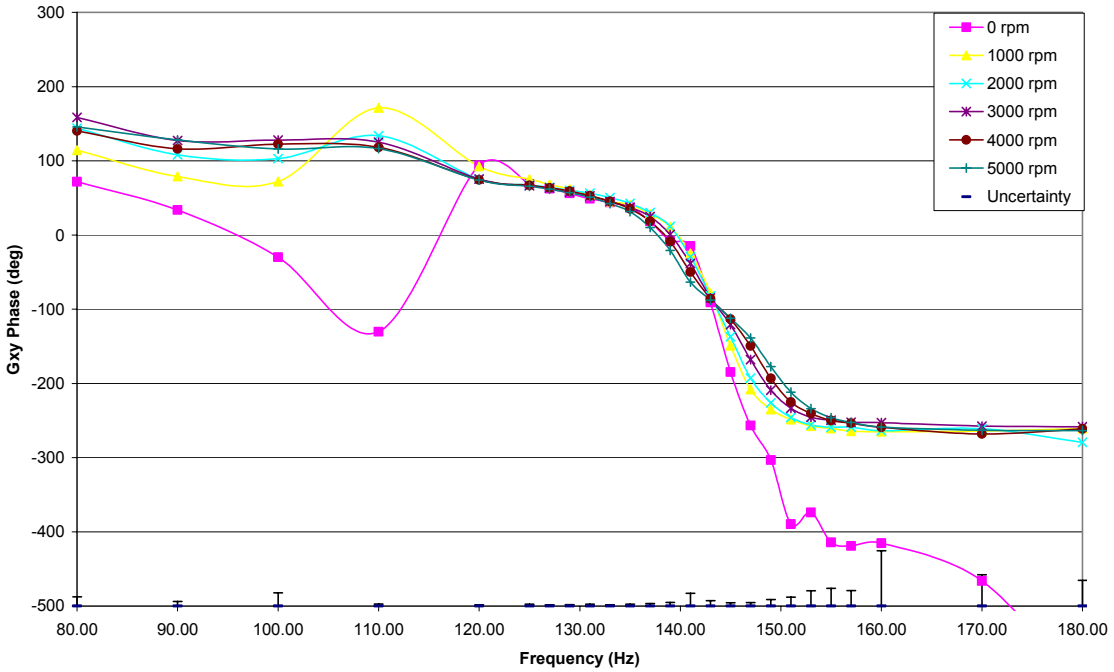

Fig. 57 G_{xy} Phase Plot

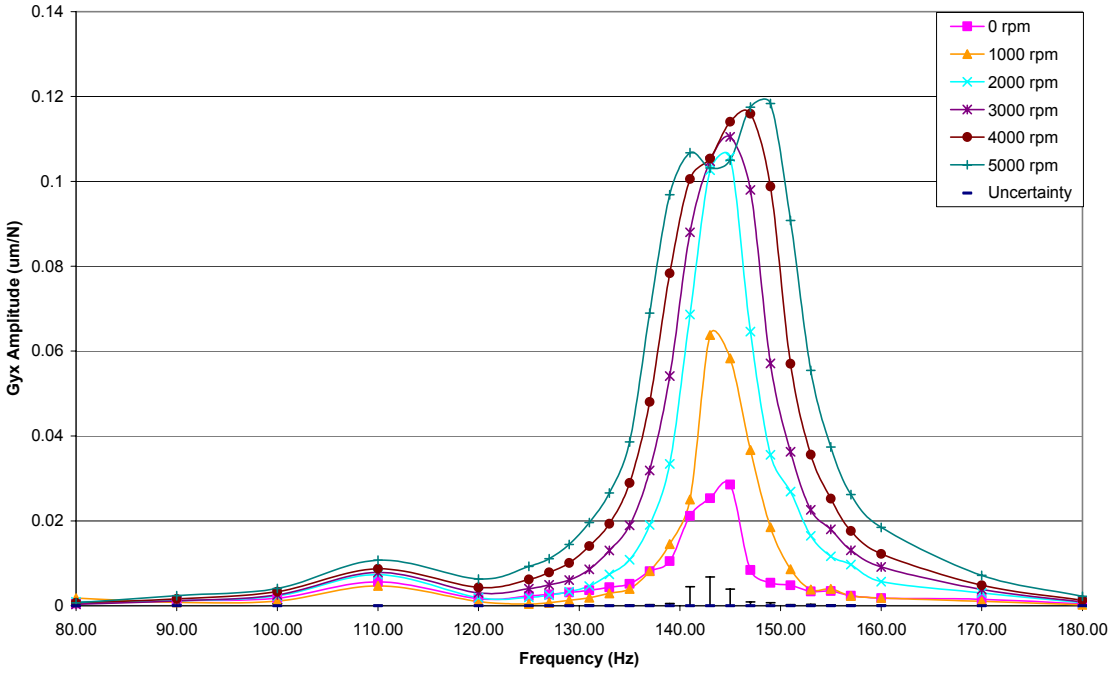

Fig. 58 G_{yx} Amplitude Plot

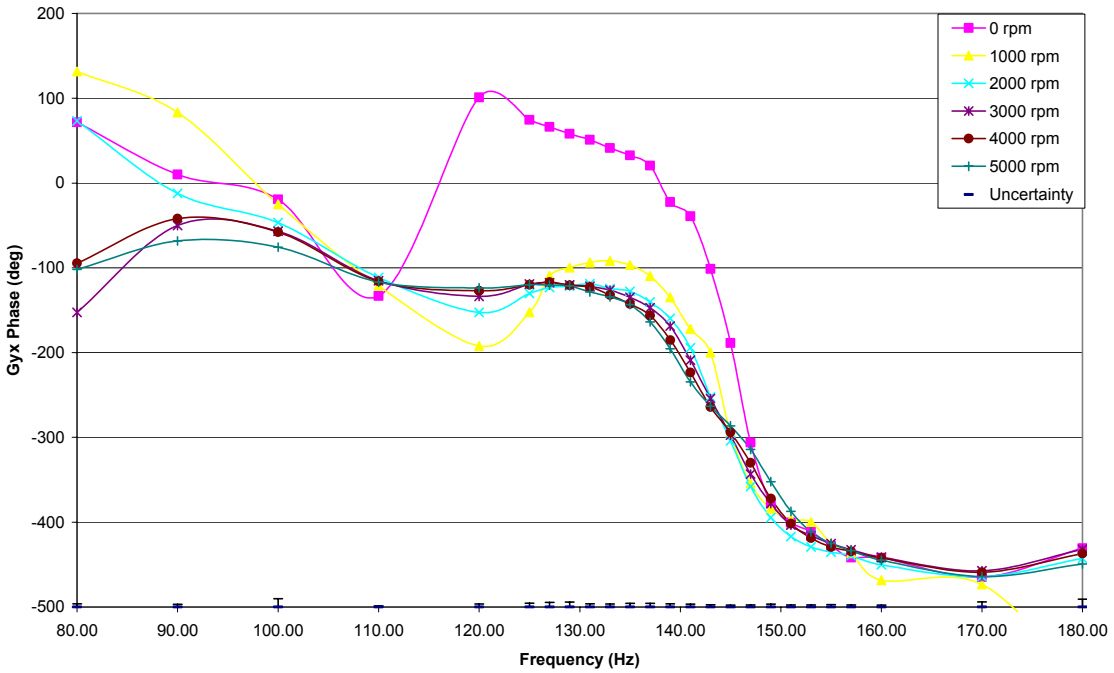

Fig. 59 G_{yx} Phase Plot

These results display the expected cross-coupling and natural frequency shifts. The cross-coupled DFTFs increase in magnitude with increasing rotor speed, particularly in the region near the natural frequencies. The decrease in the peak amplitudes of the direct terms with increasing rotor speed is predicted in the theoretical problem. The natural frequencies have separated by over 10 Hz at 5000 rpm. Figure 60 displays the damped natural frequency map from the XLTRC^2 analysis. The predicted natural frequency separation at 5000 rpm is slightly more than 10 Hz. The XLTRC^2 predictions correlate with the results of DFTF tests.

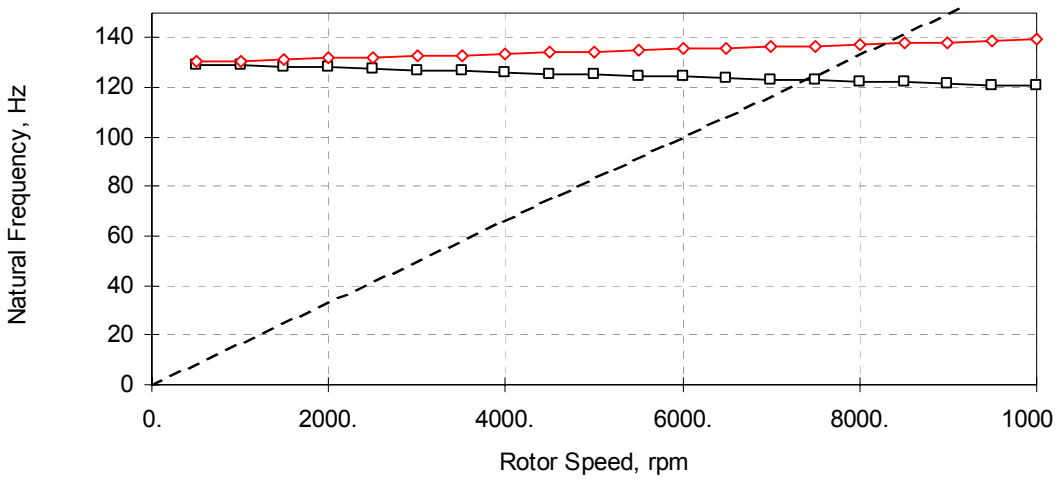

Fig. 60 Rotordynamic Damped Natural Frequency Map

Uncertainties tend to be low where flexibility is low and high where flexibility is high. This is because the forces are very low in regions of high flexibility. The small forces have an adverse effect on the signal to noise ratios. In general, the amplitude uncertainties are very good, and the DFTF curve uniformity reflects this. The phase uncertainty is somewhat more noticeable. The curves of the cross-coupled phases are not as smooth as might be expected based on the uncertainties. One possible cause of this could the position-dependent strain correction. In subtracting the strain, an error in the phase of the position-dependent strain could have a significant effect on the resulting corrected strain value. Consider two vectors of slightly different magnitude directed in roughly the same direction. Small uncertainties in the direction of either vector could

have a noticeable effect on the direction of the difference between the vectors. It is likely that the cross-coupled phases have larger uncertainties than detected by the standard deviation analysis. However uncertainties given for the amplitudes of the direct and cross-coupled terms and for the phases of the direct terms are indicative of the actual uncertainty.

V. SUMMARY, CONCLUSIONS, AND EXTENSIONS

The results of the DFTF testing are encouraging and offer support for the application of FOSG force measurements in MBs to other areas of rotordynamic testing. A summary of the background information, calibration method, and DFTF testing follows. Unusual phenomena encountered during calibration and testing are emphasized, and final conclusions are stated.

Summary of Calibration and DFTF Testing

While, historical attempts to measure forces in magnetic bearings (MBs) have been unsuccessful. FOSGs have provided a new method for measuring MB forces. They more accurate and less susceptible to noise than conventional strain gauges. FOSGs installed in a MB and have produced accurate force measurements resulting in successful rotordynamic testing. The test rig includes two MBs (only one with FOSGs) that support a rotor. The rotor consists of two disks on a flexible shaft. The disks increase the polar inertia and, accordingly, the gyroscopic properties of the system.

The FOSGs are installed in the non-drive end MB. They are calibrated with the inertial force required to translate the rotor in a radial direction. The rotor is translated with sinusoidal excitation signals in the vertical and horizontal directions. Excitation frequencies ranging from 10 Hz to 65 Hz are utilized because they are well below the first bending mode of the rotor. Tests are repeated for uncertainty analysis. FFTs of the FOSG responses and the MB proximity probes data are taken to produce amplitude and phase results. The net bearing forces are determined by calculating rotor inertial forces from the proximity probe data using a finite element code. The FOSG responses and the bearing forces produce the calibration for the FOSGs. A calibration typically exhibits an uncertainty of less than 3 N or 0.1 % of the bearing load capacity. The accuracy of the calibration decreases with time, and the deviation between two calibrations taken 30 minutes apart is typically 10 N or .3 % of load capacity.

The calibrated FOSGs produce accurate dynamic force measurements in the MBs. The MB forces and the rotor position data allow for the identification of dynamic flexibility transfer functions (DFTFs). The rotor is excited in the vertical and horizontal directions by the non-drive end (FOSG equipped) MB. Single frequency excitation signals ranging from 80 to 180 Hz are used. The rotor speed is varied from 0 rpm to 5000 rpm and repeated tests are performed for uncertainty analysis. FFTs of the MB force results and the proximity probe data are taken, and two degree-of-freedom DFTFs are calculated from the MB forces to the rotor position at the non-drive end MB. The DFTFs exhibit gyroscopic characteristics including a dramatic increasing in cross coupling and noticeable natural frequency shifts corresponding forward and backward critical speeds. Predictions from a finite element rotor model correlate with the observed natural frequency shifts. At 5000 rpm, the first bending mode natural frequencies differ by approximately 10 Hz. These results demonstrate that FOSGs in MBs can accurately test rotodynamic properties of a system.

Discussion of Unusual Phenomena

The position-dependent strain has been compensated for, but not explained. The repeatability of the position measurements and the accuracy of the FOSGs suggest that uncertainties could be reduced. These issues and possible causes are discussed in this section.

Position-Dependent Strain

Throughout the calibration and testing, the position-dependent strain has been addressed, and its effects have been removed, but its cause has not been determined. Several possible causes have surfaced. The load ratio between the primary and auxiliary poles could change with position. The load ratio change might occur when the rotor travels significantly off center. The distance between a primary pole and the rotor would not change at the same rate as the distance between its auxiliary pole and the rotor. A change in pitch could also be the cause a position-dependent strain. The laminates at

one end of the bearing would be nearer the rotor than the laminates at the other end of the bearing. In general any configuration change that affects the magnetic field distribution could create a change in the strain.

Figure 61 is a representation of the magnetic field intensity in a magnetic bearing. At first glance, it might appear that a slight change in rotor position would not produce a noticeable effect. However, because the weight of the rotor is large relative to the dynamic forces in calibration and testing, a slight change in the magnetic field could produce changes in strain on the order of those produced by the dynamic forces.

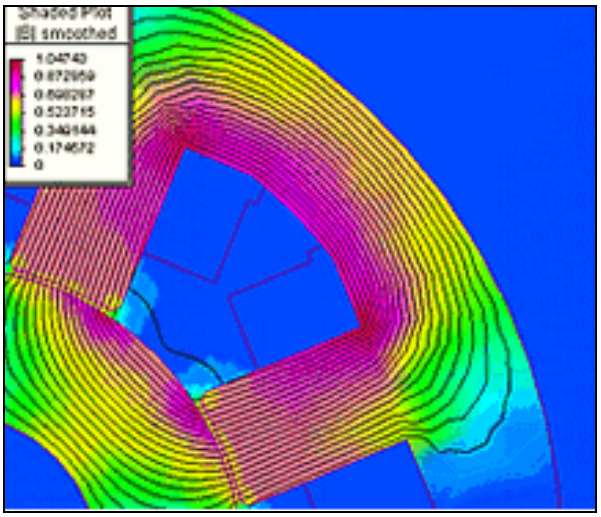

Fig. 61 Magnetic Field Intensity Inside a Magnetic Bearing [1]

Uncertainty and Repeatability Issues

The uncertainties in the FOSG calibration and the DFTF testing are acceptable. However, considering the excellent repeatability of position measurements and the accuracy of the FOSGs, the uncertainties can still be improved. There are several possible causes for uncertainty. The controller states may differ slightly for different tests. This could mean that intended net force is not always divided in the same way between opposing poles. Additionally, the FOSGs have not been thoroughly tested at the strain levels observed during testing and calibration. The bearing laminates also

exhibit signs of age such as delamination and slight corrosion. These factors may also have an impact on uncertainty.

Conclusions

Recent advances in strain gauge technology have provided an effective means of obtaining MB forces. After exploring several methods for calibrating the FOSGs, a calibration method has been developed that produces force measurements with uncertainties of less than .3% of the bearing load capacity. The calibration was successfully used to determine DFTFs. The experimental DFTF correlated with results from an XLTRC^2 mode and a theoretical example.

Force measurements from MBs have now been used to successfully detect known rotordynamic phenomena. FOSG force measurements can now be applied in situations were the results and their physical causes are not well know or understood. MBs can be used as calibrated exciters to study new areas of rotordynamics. One such use is in determining impeller coefficients for compressors. MBs already installed in these compressors could be equipped with FOSGs, and the impeller force could be measured. The applications of FOSGs in magnetic bearings are considerable, and the possibility for exploring new phenomena in rotordynamics is promising.

REFERENCES

[1] Revolve Magnetic Bearing Inc., 2003, "Magnetic Bearings: How They Work," http://www.revolve.com, Web Site accessed August 2003, Calgary, Alberta, Canada.

[2] Fiber Dynamics Inc., 2003, "Products," http://www.fiberdynamics.com, Web Site accessed August 2003, Bryan, Texas.

[3] Traxler A., Schweitzer G., 1984, *Measurement of the Force Characteristics of a Contactless Electromagnetic Rotor Bearing*, Institute for Mechanics, ETH Zurich, Switzerland.

[4] Lee C., Ha Y., Kim C., 1994, "Identification of Active Magnetic Bearing System Using Magnetic Force Measurement," *The Fourth International Symposium on Magnetic Bearings*, Zurich, pp 305-309.

[5] Matros M., Sobotzik J., Nordmann R., 1996, "A New Model-Based Method for the Accurate Measurement of Magnetic Bearing Forces," microfiches, *Fourth International Symposium on Magnetic Suspension Technology*, Gifu City, Japan, pp 239-248.

[6] Fittro R., Baun D., Maslen E., Allaire P., 1997, "Calibration of an 8-Pole Planar Radial Magnetic Actuator," ASME Paper 97-GT-18, *International Gas Turbine & Aeroengine Congress & Exhibition*, Orlando, Florida.

[7] Gahler C., 1998, "Rotor Dynamic Testing and Control with Active Magnetic Bearings," Ph.D. dissertation at ETH, Zurich, Switzerland.

[8] Knopf E., Nordmann R., 2000, "Identification of the Dynamic Characteristics of Turbulent Journal Bearings Using Active Magnetic Bearings," IMechE Paper, C576/110/2000.

[9] Pottie K., Matthijssen J., Norbart C., Gielen L., 1999, "Modal Parameter Estimation of Rotation Machinery," IMechE Paper C556/005/99.

[10] Raymer S., Childs D., 2001, "Force Measurements in Magnetic Bearings Using Fiber Optic Strain Gauges," ASME Paper 2001-GT-0027, *International Gas Turbine & Aeroengine Congress & Exhibition*, New Orleans, Louisiana.

[11] Pavesi L., Childs D., 2002, "Force Measurement in Magnetic Bearings Using Fiber Optic Strain Gauges." M.S. thesis, Texas A&M University, College Station, Texas.

[12] Childs D., 1993, *Turbomachinery Rotordynamics: Phenomena, Modeling, & Analysis*. John Wiley & Sons, Inc., New York.

VITA

Zachary Scott Zutavern was born Setpember 14, 1979 in Charlottesville, Virginia to Fred J and Victoria Ann Zutavern. His sister Brianna Lyn Zutavern was born July 19, 1982 at which time he and his family moved to Albuquerque, NM. Zachary attended Albuquerque Public Schools until graduating in 1998. For higher education, he attended Texas A&M University where he earned a B.S. in mechanical engineering, a B.A. in physics (2002), a Minor in mathematics (2002), and a Master's in mechanical engineering (2004). Zachary married Lauren Anne Allbright on May 25, 2002. They currently reside at 3911 Sioux Circle, Bryan, TX 77802 while Zachary is pursuing his Ph.D. in mechanical engineering at Texas A&M University.